

Skeleton Clustering: Dimension-Free Density-based Clustering

Zeyu Wei

Department of Statistics, University of Washington
and

Yen-Chi Chen

Department of Statistics, University of Washington

April 23, 2021

Abstract

We introduce a density-based clustering method called skeleton clustering that can detect clusters in multivariate and even high-dimensional data with irregular shapes. To bypass the curse of dimensionality, we propose surrogate density measures that are less dependent on the dimension but have intuitive geometric interpretations. The clustering framework constructs a concise representation of the given data as an intermediate step and can be thought of as a combination of prototype methods, density-based clustering, and hierarchical clustering. We show by theoretical analysis and empirical studies that the skeleton clustering leads to reliable clusters in multivariate and high-dimensional scenarios.

Keywords: high-dimensional clustering, density estimation, density-based clustering, k-means clustering

1 Introduction

Density-based clustering (Azzalini and Torelli, 2007; Menardi and Azzalini, 2014; Chacón, 2015) is a popular framework to group observations into clusters defined based on the underlying probability density function (PDF). In practice, when the PDF is unknown, the PDF is estimated via the random sample first and then the estimated PDF is used to obtain the resulting clusters. Many clustering methods have been proposed within the framework of density-based clustering. The mode clustering (Li et al., 2007; Chacón and Duong, 2013; Chen et al., 2016) find clusters via the local modes of the underlying PDF. When the kernel density estimator (KDE) is used to estimate the PDF, the mode clustering can be done easily via the mean-shift algorithm (Fukunaga and Hostetler, 1975; Cheng, 1995; Carreira-Perpinán, 2015). Another famous density-based clustering approach is the level-set clustering (Cuevas et al., 2000, 2001; Mason et al., 2009; Rinaldo et al., 2012), which creates clusters as the connected components of regions where the density is above a certain threshold. The well-known DBSCAN (Density-Based Spatial Clustering of Applications with Noise) method (Ester et al., 1996) is a special case of a level set clustering. Moreover, the cluster tree (Klemelä, 2009; Stuetzle and Nugent, 2010; Chaudhuri and Dasgupta, 2010; Chaudhuri et al., 2014; Eldridge et al., 2015; Kim et al., 2016) is a density-based clustering combining information from both modes and level-sets. This method creates a tree structure with each leaf represents a mode of the density and the tree describes the evolution of level-set clusters at different density levels.

Compared to the conventional k-means clustering (Lloyd, 1982; Hartigan and Wong, 1979; Pollard, 1982) and the model-based clustering methods (Fraley and Raftery, 2002), a density-based clustering approach is capable of finding clusters with irregular shapes and gives an intuitive interpretation based on the underlying PDF. Furthermore, the fact that clusters are defined via the underlying PDF makes it possible to view the clustering problem as an estimation problem—the clusters from the true PDF that generates the data are the parameters of interest and estimated clusters are the sample quantities utilized to approximate the underlying population clusters.

Although density-based clustering enjoys many advantages, it has a fundamental limitation: the curse of dimensionality (Scott, 2015; Wasserman, 2006). Because a density-based clustering method often involves a density estimation step, it does not

scale well with the dimension. Specifically, the convergence rate of a density estimator is $O_P(n^{-\frac{2}{4+d}})$ under usual smoothness conditions (Scott, 2015; Wasserman, 2006), and this rate will be very slow when d is large.

To overcome the curse of dimensionality and to apply density-based clustering to high-dimensional data, we borrow the idea of merging a large number of k -means clusters from (Peterson et al., 2018; Fred and Jain, 2005; Maitra, 2009; Baudry et al., 2010) and propose density-based similarity measures suitable for high-dimensional settings. The idea can be summarized as follows. We first find a large set of proto-clusters (called knots) by k -means clustering. Then we measure the similarity between knots using a density-based criterion that is estimable even in high-dimensions. These similarity measures behave like the bones connecting knots. Finally, we merge knots according to a linkage criterion to create the final clusters. Because the construction involves creating knots and bones, we call this method *Skeleton Clustering*.

To illustrate the limitation of the classical approaches and highlight the effectiveness of skeleton clustering, we conduct a simple simulation in Figure 1. It is a $d = 200$ dimensional data consisted of five components with non-spherical shapes. The actual structure is in 2-dimensional space as illustrated in Figure 1. We add Gaussian noises in other dimensions to make it a $d = 200$ dimensional data (see Section 5 for more details). Traditional k -means and spectral clustering fail to find the five components, and mean shift algorithm cannot form clusters due to the high dimensionality of the data. However, our proposed method (bottom-right panel) can successfully recover the underlying five components.

Outline. In section 2, we describe the skeleton clustering framework. In section 3, we introduce similarity measures that can be utilized in the skeleton clustering framework. In section 4, we prove the consistency of the sample similarity measures. In section 5, we present some simulation results for skeleton clustering. In section 6, we test the performance of skeleton clustering on real data. In section 7, we conclude the paper and points some directions for future research.

The R implementation of the skeleton clustering methods and some simulation codes can be founded at <https://github.com/JerryBubble/skeletonClus>

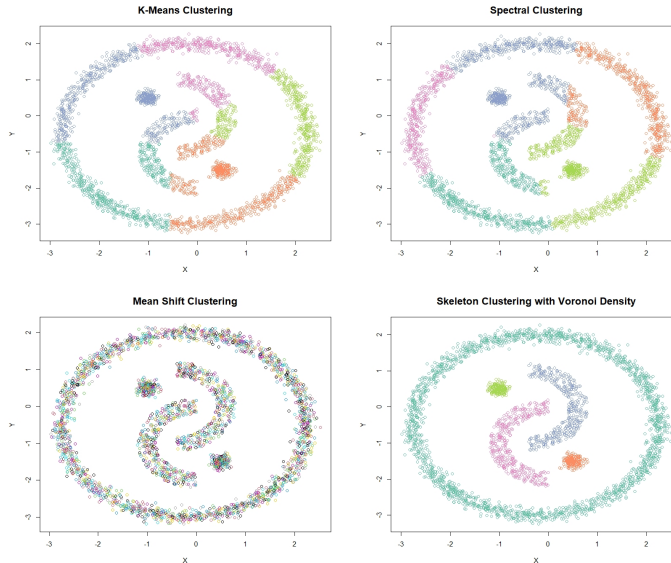


Figure 1: Yinyang Data with dimension 200. The bottom-right is clustering result with Skeleton clustering framework and using the newly proposed Voronoi density similarity measure.

Algorithm 1 Skeleton clustering

Input: Observations X_1, \dots, X_n , final number of clusters S .

1. **Knot construction.** Perform k -means clustering with a large number of k ; the centers are the knots. Generally, we choose $k = \sqrt{n}$.
 2. **Edge construction.** Apply approximate Delaunay triangulation to the knots.
 3. **Edge weights construction.** Add weights to each edge using either Voronoi density, Face density, or Tube density similarity measure (See Section 3).
 4. **Knots segmentation.** Use linkage criterion to segment knots into S groups based on the edge weights.
 5. **Assignment of labels.** Assign cluster labels to each observation based on which knot-group the nearest knot belongs to.
-

2 Skeleton Clustering Framework

In this section, we formally introduce the skeleton clustering framework. Let $\mathbb{X} = \{X_1, \dots, X_n\}$ be a random sample from an unknown distribution with density p supported on a compact set $\mathcal{X} \in \mathbb{R}^d$. The goal of clustering is to partition \mathbb{X} into clusters $\mathbb{X}_1, \dots, \mathbb{X}_S$, where S is the final number of clusters.

A summary of the skeleton clustering framework is provided in Algorithm 1. Figure 2 illustrates the overall procedure of the skeleton clustering method. Starting with a collection of observations (panel (a)), we first find knots, the representative points of the entire data (panel (b)). Then we compute the corresponding Voronoi cells induced by the knots (panel (c)) and the edges associating the Voronoi cells (panel (d), this is the Delaunay triangulation). For each edge in the graph, we compute a

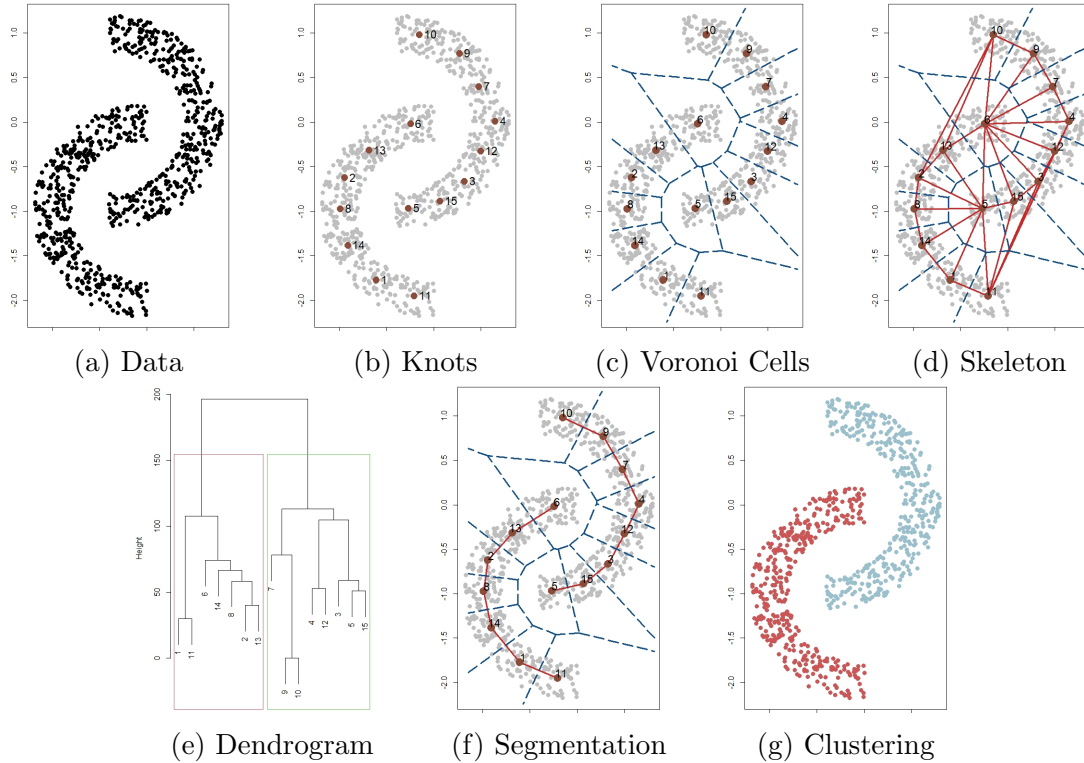


Figure 2: Skeleton Clustering illustrated by Two Moon Data ($d=2$).

density-based similarity measure that quantifies the closeness of each pair of knots. For the next step we segment knots into groups based on a linkage criterion (single linkage in this example), leading to the dendrogram in panel (e). Finally, we choose a threshold that cuts the dendrogram into $S = 2$ clusters (panel (f)) and assign cluster label to each observation according to the knot-cluster that it belongs to (panel (g)).

In summary, the skeleton clustering consists of the following five steps:

1. Knots construction.
2. Edges construction.
3. Edge weights construction.
4. Knots segmentation.
5. Assignment of labels.

In what follows in this section, we provide a detailed description of each step except Step 3. Step 3 is the key step in our clustering framework where we incorporate the information from the underlying density into clustering and we defer the detailed discussion of Step 3 to Section 3 and Section 4. We include a short analysis on the computational complexity of our skeleton clustering framework in Appendix A.

2.1 Knots Construction

The construction of knots is a step aiming at finding representative points in the data that we can use to compute density-based criterion in the later stage. The knots can be viewed as landmarks inside the data where we can shift our focus from the entire data to these local locations.

A simple but reliable approach for constructing knots is the k -means algorithm. Here, we apply the k -means algorithm with a large number k (much larger than S , the desired number of final clusters), and this procedure behaves like overfitting the k -means. Notably, we do not use k -means procedure to obtain final clustering, but instead we use it as a way to find concise representations of the original data. In panel (a) of Figure 2, the knots constructed by overfitting k -means form a concise representation of the original data.

The number of knots k is a key parameter in the knots construction step. It controls the trade-off between the quality of data representation and the reliability of each knot. More knots can give better representation of the data, but, if we have too many knots, the number of observation per knot will be small, so the uncertainty in estimation in the later stage will be large. We find that a simple reference rule $k = \lceil \sqrt{n} \rceil$ (rounding \sqrt{n} to the nearest integer) works very well in our empirical studies. While this reference rule seems to be reliable, we would recommend to examine the knot-size distribution (Figure 3, for more plots see Appendix C.2) before making the final decision. The knot-size distribution is the empirical distribution size of each knot (number of observation of each knot) with a given choice of k . This distribution is useful because the density-based weights (in Step 3) are estimated by the data within each pair of knots, with the effective sample size be the size of the two knots being assessed. A balanced knot-size distribution ensures the estimated edge weights are all reliable.

In this work we use overfitting k -means as the default way for knots construction, but there are alternative approaches to find knots such as subsampling, the other coresets construction methods (Bachem et al., 2017), and the Self-Organizing Maps (SOM) (Heskes, 2001). We show in Appendix C.3 that the SOM can also be used to find knots but the performance is slightly worse than the idea of overfitting k -means.

Remark 1. Since k -means algorithm does not always find the global optimum, we will repeat it many times with random initial points (generally 1,000 times or more) and choose the

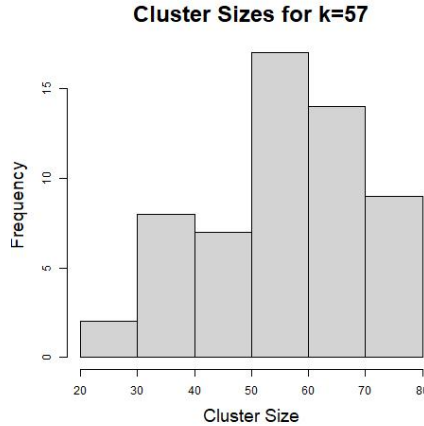


Figure 3: The knot-size diagram: a histogram of cluster sizes given by k -means with $k = \lfloor \sqrt{n} \rfloor$ on Yinyang data with dimension 200; see Section 5.1.1 for more details.

one with the optimal objective function. This works well for all of our numerical analysis. Moreover, since we are only using k -means as a tool to find a useful representation, we do not need to find the actual global optimum. All we need is a set of knots forming a useful representation.

2.2 Edges construction

With the constructed knots, the next step is to find the edges connecting these knots. Let c_1, \dots, c_k be the knots from the first step and we use $\mathcal{C} = \{c_1, \dots, c_k\}$ to denote the collection of them. We add an edge between a pair of knots if they are neighboring with each other, with the neighboring condition referring to that the corresponding Voronoi cells share a common boundary (Voronoi, 1908). The Voronoi cell, or Voronoi region, \mathbb{C}_j , associated with knot c_j is the set of all points in \mathcal{X} whose distance to c_j is the smallest compared to other knots. That is,

$$\mathbb{C}_j = \{x \in \mathcal{X} : d(x, c_j) \leq d(x, c_l) \quad \forall l \neq j\},$$

where $d(x, y)$ is the usual Euclidean distance. Therefore, we add an edge between knots (c_i, c_j) if $\mathbb{C}_i \cap \mathbb{C}_j \neq \emptyset$. Such resulting graph is the Delaunay triangulation (Delaunay, 1934) of the set of knots \mathcal{C} and we denote it as $DT(\mathcal{C})$. In a nutshell, the skeleton structure in our clustering framework is given by the Delaunay triangulation of \mathcal{C} .

The Delaunay triangulation graph is conceptually intuitive and appealing, but empirically the computational complexity of the exact Delaunay triangulation algo-

rithm has an exponential dependence on the ambient dimension d (Amenta et al., 2007; Chazelle, 1993). Given our high-dimensional data setting, exact Delaunay triangulation is empirically unfavorable. Therefore, in practice, we approximate the Delaunay Triangulation with $\widehat{DT}(\mathcal{C})$ by only looking at the 2-nearest knots of the sample data. Note that there is an edge in the Delaunay triangulation between two knots c_i, c_j if the corresponding Voronoi cells share a boundary, and hence there is a non-empty region of points whose 2-nearest knots are c_i, c_j . Therefore, for approximation, we query the two nearest knots for each data point and have an edge between c_i, c_j if there is at least one data point whose two nearest neighbors are c_i, c_j . The complexity of the neighbor search depends linearly on the dimension d , which is desirable for high-dimensional setting (Weber et al., 1998). Conceptually such approximation identifies two knots to be neighboring if they have some sample points in between, and this sample-based approximation to the Delaunay Triangulation has reliable empirical performance.

2.3 Edge weight construction

With the edges and knots from the previous sections, we assign each edge with a weight that represents the similarity/closeness of the pair of knots. In this work, we use density-based quantities as the weights in our skeleton clustering framework. Since the description of the similarity measures is more involved, we defer the detailed discussion of the similarity measures to the next section (Section 3). It is worth noting here that the similarity measures proposed in this work are estimated based on surrogates of the underlying density function and the estimation procedure has minimal dependence on the ambient dimension. Therefore, the estimations of the newly proposed similarity measures are reliable even under high-dimensional setting (see theoretical analysis in Section 4).

2.4 Knots Segmentation

Given the edge weights, the next step is to partition the knots into the desired number of clusters. We use the idea of hierarchical clustering in this step. While hierarchical clustering is often applied to a distance matrix rather than a similarity matrix, we can use the inverse of the similarity as the distance.

Hierarchical clustering requires a linkage criterion to determine how to merge

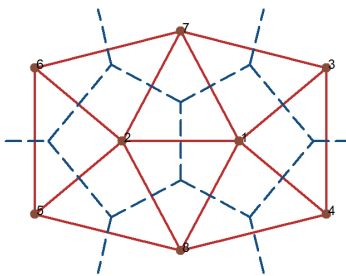


Figure 4: Delaunay Triangulation and Voronoi Tessellation.

knots, and we find that single linkage generally gives a reliable result when there are no overlapping clusters. Due to the use of knots and density-based weights, the single linkage here also leads to clusters that are robust against noises (see Section 5.2). When there are overlapping clusters, our simulation studies show that the average linkage works better (see Section 5.3).

The number of final clusters S can be unknown but is an essential parameter for hierarchical clustering to apply. The dendrograms given by hierarchical clustering can be a helpful tool in this situation, displaying the clustering structure at different resolutions. Consequently, analysts can choose a cut that preserves the meaningful structures based on the dendrograms.

Remark 2. Although the dendrograms for knots given by our method are not exactly the cluster trees, the pruning graph cluster tree procedure proposed in (Nugent and Stuetzle, 2010) with excess mass can also be applied to help decide the final segmentation. (Peterson et al., 2018) also presented similar ideas choosing the final number of clusters by looking at the lifetime of the clusters in the dendrogram. Additionally, the traditional “elbow” methods can be used to determine the number of clusters. An inferential choice of the number of clusters can also be made using the gap statistics (Tibshirani et al., 2001).

2.5 Assignment of labels

In the previous step, we have created S groups of knots and each group has a cluster label. To pass the cluster membership to each observation, we assign the label to each observation according to which group its nearest knot belongs to. For instance, if an observation X_i is closest to knot c_j and c_j belongs to cluster ℓ , we assign cluster label ℓ to observation X_i . This step assigns a cluster label to every observation.

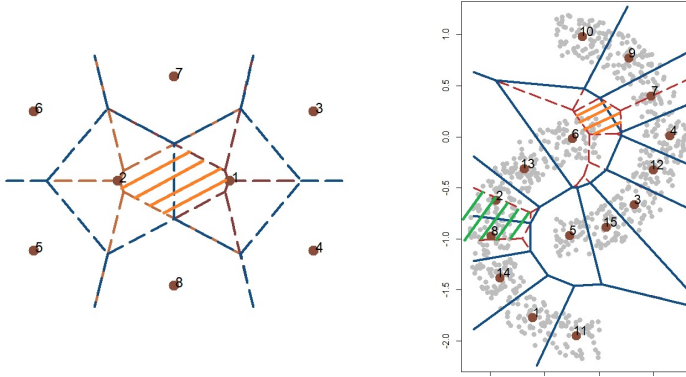


Figure 5: **Left:** Orange shaded area illustrates the 2-NN region of knots 1, 2. **Right:** Shaded areas illustrate the 2-NN region of knots 6, 7 and knots 2, 8.

3 Density-based Edge Weights Construction

To incorporate the information of density into clustering, we calculate the edge weights based on the underlying density function. However, the conventional notion of PDF is not feasible in multivariate data due to the curse of dimensionality. To resolve this issue, we introduce three density-related quantities that are estimable even when the dimension is high.

3.1 Voronoi Density

The Voronoi density measures the similarity between a pair of knots (c_j, c_ℓ) based on the total number of observations whose 2-nearest knots are c_j and c_ℓ . We start with defining the Voronoi density based on the underlying probability measure and then introduce its sample analog.

Given a metric d on \mathbb{R}^d , the 2-Nearest-Neighbor (2-NN) region of a pair of knots (c_j, c_ℓ) is defined as

$$A_{j\ell} = \{x \in \mathcal{X} : d(x, c_i) > \max\{d(x, c_j), d(x, c_\ell)\}, \forall i \neq j, \ell\}.$$

In this work we take $d(., .)$ to be usual Euclidean distance and use $\|\cdot\|$ to denote the Euclidean norm. The set $A_{j\ell}$ describes the region where c_j and c_ℓ are the two closest knots and is illustrated in the left Figure 5.

Following the idea of density-based clustering, two knots c_j, c_ℓ belongs to the same clusters if they are in a connected high-density region of the PDF, and we would expect the region between c_j, c_ℓ to have a high density. Hence, the probability $\mathbb{P}(A_{j\ell}) = P(X_1 \in A_{j\ell})$ measures the association between c_j and c_ℓ (see Figure 5

right). Based on this insight, the *Voronoi density (VD)* measures the edge weight of (c_j, c_ℓ) with

$$S_{j\ell}^{VD} = \frac{\mathbb{P}(A_{j\ell})}{\|c_j - c_\ell\|}. \quad (1)$$

Namely, we divide the probability of overlapping region by the mutual Euclidean distance. The division of the distance adjusts for the fact that 2-NN regions have different sizes and provides more weights to edges between knots that are close to each other.

In practice we estimate $S_{j\ell}^{VD}$ by a sample average. Specifically, the numerator $\mathbb{P}(A_{j\ell})$ is estimated by $\widehat{P}_n(A_{j\ell}) = \frac{1}{n} \sum_{i=1}^n I(X_i \in A_{j\ell})$ and the final estimator for the VD is constructed as

$$\widehat{S}_{j\ell}^{VD} = \frac{\widehat{P}_n(A_{j\ell})}{\|c_j - c_\ell\|}. \quad (2)$$

Note that here we are assuming that c_1, \dots, c_k are given beforehand. If they are estimated by the data as well, we replace them by the sample analog $\widehat{c}_1, \dots, \widehat{c}_k$ and replace the region $A_{j\ell}$ by $\widehat{A}_{j\ell}$.

The Voronoi density can be computed in a fast way. The numerator, which only depends on 2-nearest-neighbors calculation, can be computed efficiently by the k-d tree algorithm (Bentley, 1975). For high-dimensional space, space partitioning search approaches like the k-d tree can be inefficient, but a direct linear search still gives short run-time (Weber et al., 1998). The denominator requires distance calculation and can be burdensome in a high-dimensional setting, but note that we only need to calculate the distance for edges present in $\widehat{DT}(\mathcal{C})$, which is far less than $k(k-1)/2$, where k is the number of knots. Hence, the Voronoi density calculation can always be carried out in a fast way even for high-dimensional data with large sample size.

3.2 Face Density

Here we present another density-based quantity to measure the similarity between two knots. Since the Voronoi cell of a knot describes the region associated with the knot, a natural way to measure similarity between two knots is to investigate the shared boundary of the corresponding Voronoi cells. If two knots are highly similar, we would expect the boundary to lie in high-density region and to be surrounded

by many observations. Based on this idea, we define the *Face Density (FD)* as the integrated PDF over the “face” (boundary) region. Note that although the density is involved in FD, by integrating over the face region the problem essentially reduces to a 1-dimensional density estimation task regardless of the dimension of the ambient space. Formally, let the face region between two knots c_j, c_ℓ be $F_{j\ell} = \mathbb{C}_j \cap \mathbb{C}_\ell$. At the population level, the FD is defined as

$$S_{j\ell}^{FD} = \int_{F_{j\ell}} p(x) \mu_{d-1}(dx) = \int_{F_{j\ell}} d\mathbb{P}(x), \quad (3)$$

where $\mu_s(dx)$ is the s -dimensional volume measure.

To estimate the FD, we utilize the idea of kernel smoothing in combination with data projection. By the construction of the Voronoi diagram, the boundary of two regions is orthogonal to the line passing through the two corresponding knots (we call it the ‘central line’) and intersects the central line at the middle point regardless of the dimension of the data (see Figure 4 for reference). Therefore, we estimate the FD by projecting observations onto the central line, performing 1-dimensional kernel density estimation (KDE) along the central line, and evaluating the density at the midpoint. Specifically, fix two knots c_j, c_ℓ , let $\mathbb{C}_j, \mathbb{C}_\ell$ be the closure of the corresponding Voronoi cells, and denote $\Pi_{j\ell}(x)$ as the projection of $x \in \mathcal{X}$ onto the central line passing through c_j and c_ℓ , we define the estimator $\widehat{S}_{j\ell}^{FD}$ to be

$$\widehat{S}_{j\ell}^{FD} = \frac{1}{nh} \sum_{X_i \in \mathbb{C}_j \cup \mathbb{C}_\ell} K\left(\frac{\Pi_{j\ell}(X_i) - (c_\ell + c_j)/2}{h}\right) \quad (4)$$

where K is a smooth, symmetric kernel function such as Gaussian kernel and $h > 0$ is the smoothing bandwidth that controls the amount of smoothing. It is noteworthy that, while the conventional kernel smoothing suffers from the curse of dimensionality (Chen, 2017; Chacón et al., 2011; Wasserman, 2006), we will later show that the kernel estimator in equation (4) does not suffer from the curse of dimensionality (Theorem 2).

3.3 Tube Density

While FD is conceptually appealing, the characterization of the face (the boundary between two Voronoi cells) could be challenging since the shapes of the faces may be irregular. Here we propose a measure similar to face density but has a predefined regular shape. For a point x , we define the disk area centered at x with radius R and

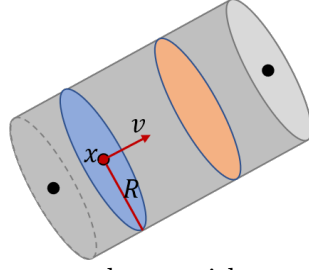


Figure 6: The disk area centered at x with a radius R and a direction ν .

normal direction ν as

$$\text{Disk}(x, R, \nu) = \{y : \|x - y\| \leq R, (x - y)^T \nu = 0\};$$

see Figure 6 for an illustration of the disk area.

To measure the similarity between knots c_j and c_ℓ , we examine the integrated density within the disk areas along the central line. In more details, the central line can be expressed as $\{c_j + t(c_\ell - c_j) : t \in [0, 1]\}$, and any point on the central line can be written as $c_j + t(c_\ell - c_j)$ for some t . For a point $c_j + t(c_\ell - c_j)$, we define the integrated density in the disk region (called disk density) as

$$\text{pDisk}_{j\ell, R}(t) = \mathbb{P}(\text{Disk}(c_j + t(c_\ell - c_j), R, c_\ell - c_j)) = \int_{\text{Disk}(c_j + t(c_\ell - c_j), R, c_\ell - c_j)} p(x) dx.$$

The *Tube density (TD)* measures the similarity between c_j and c_ℓ as the minimal disk density along the central line, i.e.,

$$S_{j\ell}^{TD} = \inf_{t \in [0, 1]} \text{pDisk}_{j\ell, R}(t).$$

In other words, with given c_j, c_ℓ , we survey all disk density along their central line and retrieve the infimum as the similarity measure between two knots. Since the regions being surveyed together form a tube, we call it the Tube density.

For simplicity, in this work we set R to be the same for all pair of knots, but it could be chosen adaptively for each pair. In practice, we recommend the reference rule that R to be the average variance within each Voronoi cell. Our empirical studies show that this rule leads to a good performance. Theoretical analysis also shows that this reference rule for R leads to the consistency of the sample analog of the TD.

Similar to the FD, we estimate the TD by a projected KDE. Let $\Pi_{j\ell}(x)$ be the

projection of a point x on the line through c_j, c_ℓ . We first estimate the **pDisk** via

$$\widehat{\text{pDisk}}_{j\ell,R}(t) = \frac{1}{nh} \sum_{i=1}^n K\left(\frac{\Pi_{j\ell}(X_i) - c_j - t(c_\ell - c_j)}{h}\right) I(\|X_i - \Pi_{j\ell}(X_i)\| \leq R)$$

and then estimate the TD as

$$\widehat{S}_{j\ell}^{TD} = \inf_{t \in [0,1]} \widehat{\text{pDisk}}_{j\ell,R}(t). \quad (5)$$

where the infimum is approximated by grid search.

3.4 Bandwidth Selection

The estimations of the FD and the TD involve the use of the projected kernel density estimation, for which the type of kernel and the bandwidth need to be specified. Similar to the usual KDE, the kernel function does not affect the final performance much, so by default we use the Gaussian kernel in all of our experiments. It is worth noting that using the uniform kernel can save some computation since it has a compact support, but empirically we find using the Gaussian kernel leads to better final clustering results. In what follows, we focus on the bandwidth selection.

It is known that the bandwidth is a pivotal parameter that can significantly affect the estimation result of a kernel density estimator. In Figure 7, we conduct a simulation using the Yinyang data ($d = 1000$; see Section 5.1.1 for more details) and compare the performance of three common bandwidth selectors: the normal scale bandwidth (NS) (Chacón et al., 2011), the least-squared cross-validation (LSCV) (Bowman, 1984; Rudemo, 1982), and the plug-in approach (PI) (Wand and Jones, 1994). We allow each edge to have its own bandwidth. We found that the NS performs reliably well while the others may have unstable performance. As a result, we recommend using the NS as the default bandwidth selector. Additionally, since the FD and TD are both 1-dimensional density, in practice we can examine the estimated density long the central line to determine if we are oversmoothing or undersmoothing and manually adjust the bandwidth.

In addition to different bandwidth selectors, we also study how the bandwidth should depend on the sample size for clustering purpose. In 1-dimensional data, the normal scale bandwidth agrees with Silverman’s rule of thumb (Silverman, 1986) giving the bandwidth as $h = \frac{4}{3} \widehat{\sigma} n_{loc}^{-1/5}$, where $\widehat{\sigma}$ is the standard deviation of the

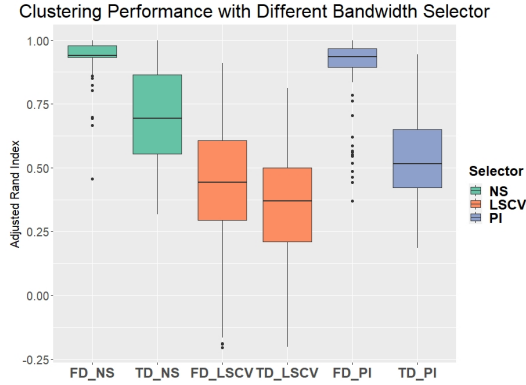


Figure 7: Performance of skeleton clustering on Yinyang data $d = 1000$ with Face and Tube density by different bandwidth selectors.

sample used in the edge weight calculation, and n_{loc} the number of sample points used. Empirically we tested the clustering performance with FD and TD calculated under bandwidth with rates on n_{loc} from $-1/3$ to $-1/10$ (see Appendix C.1). We found that the clustering performance with FD and TD generally stays stable with varying bandwidth rates, although a larger bandwidth (slower rate than $O(n_{loc}^{-1/5})$) may give better clustering results with TD when the dimension of the data is high.

4 Asymptotic Theory of Edge Weight Estimation

In our previous simulation results (Figure 1 and 7), we saw that the skeleton clustering method based on the newly proposed density-based similarity measures works well even when the dimension d is large. Here we analyze the theoretical properties of these similarity measures and use the theories to explain why these methods are effective.

We assume the set of knots $\mathcal{C} = \{c_1, \dots, c_k\}$ is given and non-random to simplify the analysis. Note that this implies the corresponding Voronoi cells $\mathbb{C} = \{\mathbb{C}_1, \dots, \mathbb{C}_k\}$ are fixed as well. We allow $k = k_n$ to grow with respect to the sample size n . All proofs are deferred to Appendix B.

4.1 Voronoi Density

We start with the convergence rate of the VD. We consider the following condition:

- (B1) There exists a constant c_0 such that the minimal knot size $\min_{(j,\ell) \in E} \mathbb{P}(A_{j\ell}) \geq \frac{c_0}{k}$ and $\min_{(j,\ell) \in E} \|c_j - c_\ell\| \geq \frac{c_0}{k^{1/d}}$.

Here $(j, \ell) \in E$ means that there is an edge between knots c_j, c_ℓ in the Delaunay Triangulation. Condition (B1) is a condition requiring that no Voronoi cell $A_{j\ell}$ has a particularly small size and all edges have sufficient length. This condition is mild because when the dimension of data d is fixed, the total number of edges of the Delaunay triangulation of k points scale at rate $O(k)$. Because the volume shrinks at rate $O(k^{-1})$, the distance is expected to shrink at rate $O(k^{-1/d})$.

Theorem 1 (Voronoi Density). Assume (B1). Then for any pair $j \neq \ell$ that shares an edge, the similarity measure based on the Voronoi density satisfies

$$\left| \frac{\widehat{S}_{j\ell}^{VD}}{S_{j\ell}^{VD}} - 1 \right| = O_p \left(\sqrt{\frac{k}{n}} \right),$$

when $n \rightarrow \infty, k \rightarrow \infty, \frac{n}{k} \rightarrow \infty$.

Theorem 1 provides the convergence rate of the sample-based Voronoi density to the population version Voronoi density. This result is reasonable because when the knots \mathcal{C} are given, the randomness in the sample-based Voronoi density is just the empirical proportion in each cell, so it is a square-root-rate estimator based on the effective local sample size n/k . Consequentially, Theorem 1 suggests that estimating the Voronoi density is easy in multivariate case when the knots are given—there is no dependency with respect to the ambient dimension.

4.2 Face Density

We now derive the convergence rate of the FD estimator. Recall that μ_d is the Lebesgue measure on the d -dimensional Euclidean space, let $F_{j\ell} = \mathbb{C}_\ell \cap \mathbb{C}_j$ denote the face region between knots c_j, c_ℓ , and let $\partial F_{j\ell}$ be the boundary of $F_{j\ell}$. We consider the following assumptions:

(D1) (Density conditions) The PDF p has compact support \mathcal{X} , is bounded away from zero that $\inf_{x \in \mathcal{X}} p(x) \geq p_{\min} > 0$, $\sup_{x \in \mathcal{X}} p(x) \leq p_{\max} < \infty$, and is Lipschitz continuous.

(B2) There exist constants c_0, c_1 such that the face area

$$\frac{c_0}{k^{1-\frac{1}{d}}} \leq \min_{(j,\ell) \in E} \mu_{d-1}(F_{j\ell}) \leq \max_{(j,\ell) \in E} \mu_{d-1}(F_{j\ell}) \leq \frac{c_1}{k^{1-\frac{1}{d}}}$$

(B3) There exists a constant c_2 such that $\max_{(j,\ell) \in E} \mu_{d-2}(\partial F_{j\ell}) \leq \frac{c_2}{k^{1-\frac{2}{d}}}$,

(B4) There is an angle $\theta_0 < \pi$ such that, for every pair of intersecting face regions F_{ij} and $F_{j\ell}$, the maximal principle angle between the two subspaces $\theta_{ij,j\ell}$ satisfies $\theta_{ij,j\ell} \leq \theta_0$

(K1) (Kernel function conditions) The kernel function K is a positive and symmetric function satisfying $\int K^2(x)dx < \infty$, $\int |x|K(x)dx < \infty$, $\int x^2K(x)dx < \infty$.

Assumption (D1) is a commonly assumed for the density estimation problem, but usually with higher-order smoothness conditions. Notably, for consistency of FD estimator we require only the Lipschitz condition since the bias of the sample estimator will be dominated by a geometric difference even if we have a higher-order smoothness (see the discussion after Theorem 2 and the Appendix B for more detail). Condition (B2) restricts the shared boundary of two Voronoi cells to scale at the rate of $O(k^{1-\frac{1}{d}})$. While this condition may seem abstract, it is a mild condition. To illustrate this, suppose we have $k = m^d$ points that are on a uniform grid of $[0, 1]^d$ for some integer m . We form the Voronoi cells of these (grid) points. The $(d - 1)$ -dimensional volume of the shared boundary of two neighboring Voronoi cells will scale at rate $O(k^{1-\frac{1}{d}})$ as $k \rightarrow \infty$. (B3) requires the boundaries of the face regions to scale at most at a rate of $O(k^{1-\frac{2}{d}})$, and (B4) requires that we cannot have two nearby faces to be parallel to each other. Assumptions (B3) and (B4) are needed when bounding the geometric difference between the estimator and the population quantity and are both mild conditions: When the knots form a spherical packing of a smooth region, these conditions hold. Notably, (D1) and (B2) imply (B1) and hence the consistency of FD requires more conditions than the consistency of VD. The condition (K1) is a common assumption on the kernel function (Wasserman, 2006; Scott, 2015) satisfied by many common kernel functions, including Gaussian kernel.

Theorem 2 (Face Density). Assume (D1), (K1), and (B2-B4). With $h \rightarrow 0$, $k \rightarrow \infty$, $hk^{1/d} \rightarrow 0$, $\frac{nh}{k^{1-\frac{1}{d}}} \rightarrow \infty$, then for any pair $j \neq \ell$, we have

$$\left| \frac{\widehat{S}_{j\ell}^{FD}}{S_{j\ell}^{FD}} - 1 \right| = O(hk^{1/d}) + O_p\left(\sqrt{\frac{k^{1-\frac{1}{d}}}{nh}}\right).$$

Theorem 2 shows the convergence rate of estimating the FD. Roughly speaking, the rate is similar to a 1-dimensional density estimation problem. With $d \rightarrow \infty$, we

have the rate to be $O(h) + O_p\left(\sqrt{\frac{k}{nh}}\right) = O(h) + O_p\left(\sqrt{\frac{1}{n_{loc}h}}\right)$, where $n_{loc} = O\left(\frac{n}{k}\right)$ is the local effective sample size. Therefore, the effect of the ambient dimension is negligible when d is large. This is because we are estimating a ‘projected’ density on the central line. When the data is projected onto the central line, the problem reduces to a 1-dimensional problem.

Noticeably, the bias term in Theorem 2 is of the order $O(h)$. While this rate is optimal under the Lipschitz smoothness (D1) for density estimation problem, it is slower than the conventional rate $O(h^2)$ when we have bounded second-order derivative of p . One may be wondering if higher-order smoothness of p is assumed, can we improve the convergence rate? Unfortunately, even if p is very smooth, the bias rate will still stay the same at $O(h)$. This is because there are two sources of bias. The first one is the usual bias from kernel smoothing, which can be improved to higher-order if we have high-order derivatives of p . The other source of bias comes from the different shapes of the Voronoi cells \mathbb{C}_j and \mathbb{C}_ℓ (for illustration see Figure 20 in Appendix B). Consider the characterization of central line as $c_j + t(c_\ell - c_j)$ for $t \in [0, 1]$, and the boundary will occur at $t = \frac{1}{2}$. Regions projected on to the central line will be different depending on the value of t . Specifically, when $t > \frac{1}{2}$, the projected region is from \mathbb{C}_ℓ whereas when $t < \frac{1}{2}$, the projected region is from \mathbb{C}_j , and those projected regions can have shapes different from the face region. This difference leads to an additional geometric bias of the order $O(h)$ and cannot be improved by higher-order smoothness of p .

From Theorem 2, one can see that the optimal bandwidth scales at rate $h \asymp \left(\frac{k^{1-3/d}}{2n}\right)^{1/3}$. Recall that our reference rule sets $k = \sqrt{n}$ so that $n_{loc} = \frac{n}{k} = \sqrt{n}$ is the average number of observations per each knot. When d large, $\frac{3}{d}$ is negligible. Thus, the optimal bandwidth is given by $h \asymp \left(\frac{k}{n}\right)^{1/3} = n_{loc}^{-1/3}$. While our empirical rule $n_{loc}^{-1/5}$ is not optimal in this case, it still gives to a consistent estimator and our empirical analysis shows that such choice leads to reliable clustering results; see Appendix C.1.

One may notice that a small k in Theorem 2 leads to a better convergence rate, which suggests to use a small k . While this is true from the perspective of estimation, a small k may lead to a bad clustering performance. Empirical results show that we need a sufficiently large number of knots to represent the data in order for the skeleton clustering to perform appropriately. Therefore, our reference rule with $k = \sqrt{n}$ is a suitable balance between the trade-off between representation and estimation. We

include an empirical analysis on the effect of k on clustering performance in Appendix C.2.

4.3 Tube Density

We now derive the convergence rate of the TD estimator. We consider the following assumptions, which are slightly stronger than the corresponding ones in the case of the FD:

- (D2) (Density conditions) The PDF p has a compact support and is 3-Hölder and $\inf_{x \in \mathcal{X}} p(x) \geq f_{\min} > 0$.
- (D3) (Disk Density conditions) For any pair c_j, c_ℓ , the minimum disk density location $t^* = \operatorname{argmin}_{t \in [0,1]} \mathbf{pDisk}_{j\ell,R}(t) \in (0, 1)$ is unique and the second derivative of the disk density $\mathbf{pDisk}_{j\ell,R}^{(2)}(t^*) \geq c_{\min} > 0$.
- (K2) (Kernel function conditions) The kernel function K is a positive and symmetric function satisfying $\int x^2 K^{(\alpha)}(x) dx < \infty$, $\int (K^{(\alpha)}(x))^2 dx < \infty$, for all $\alpha = 0, 1, 2$, where $K^{(\alpha)}$ denotes the α -th order derivative of K .

(D2) is a stronger version of (D1) that we require additional smoothness condition of p . We need the 3-Hölder class (slightly weaker than the requirement of third-order derivatives) to obtain the rate of estimating the minimum (Chacón et al., 2011; Chen et al., 2016). Also, a stronger condition (K2) on the kernel function is needed to ensure the gradient estimation is consistent. Fortunately, common kernel functions such as the Gaussian kernel satisfy these conditions.

Theorem 3 (Tube Density Consistency). Assume (D2), (D3), and (K2). Let $h \rightarrow 0$, $k \rightarrow \infty$, $R \rightarrow 0$, $nh^3 \rightarrow \infty, nhR^{d-1} \rightarrow \infty$. Suppose that for every pair c_j, c_ℓ , $\inf_{t \in [0,1]} \mathbf{pDisk}_{j\ell,R}(t)$ and $\inf_{t \in [0,1]} \widehat{\mathbf{pDisk}}_{j\ell,R}(t)$ do not occur at the boundary $t = 0, 1$. Then for any pair $j \neq \ell$ that shares an edge, we have

$$\begin{aligned} \mathbf{pDisk}_{j\ell,R}(t) &= O(R^{d-1}), \\ \left| \frac{\widehat{S}_{j\ell}^{TD}}{S_{j\ell}^{TD}} - 1 \right| &= O(h^2) + O_p\left(\sqrt{\frac{1}{nhR^{d-1}}}\right) + O_p\left(\frac{1}{nh^3}\right) \end{aligned}$$

Theorem 3 shows that the TD estimator converges to the population TD with a rate consisting of three components. We allow $R \rightarrow 0$ as $n \rightarrow \infty$ but this result also applies to scenarios where R is fixed. The first component $O(h^2)$ is the usual smoothing bias. The second component $O_p\left(\sqrt{\frac{1}{nh}}\right)$ is similar to the stochastic variation part from usual KDE but with additional dependence on R^{d-1} . This is due to the fact that, when $R \rightarrow 0$, we are using fewer and fewer observations to perform smoothing, and nR^{d-1} serves as the effective sample size. The third component $O_p\left(\frac{1}{nh^3}\right)$ is due to the error of estimating the location of the minimum. It is a squared term because the density behaves like a quadratic function around its minimum due to (D3).

While the convergence rate of TD requires stronger conditions (D2) and (K2) compared to the conditions (D1) and (K1) in estimating the FD, the TD estimator has a smaller bias than the FD estimator (comparing Theorem 2 and 3). This is because the TD is evaluated on a “regular shape”, which leads to a smoother quantity being estimated.

For the stochastic variation part, the second term in Theorem 3 gives $O_p\left(\sqrt{\frac{1}{nhR^{d-1}}}\right)$ while the second term in Theorem 2 gives $O_p\left(\sqrt{\frac{k^{1-\frac{1}{d}}}{nh}}\right)$. Note that empirically we choose R to be the average variance of the Voronoi cells, which is of order $O(k^{-1/d})$ with balanced cells. Hence $k^{1-1/d}$ and $\frac{1}{R^{d-1}}$ are at the same rate and the stochastic variation part given by the change in density are comparable for TD and FD estimators. However, for TD we have another source of variation coming from the uncertainty of the location of minimum, which can cause TD to have larger variation than the FD estimator.

Based on the above reasoning, our choice of R leads to $\frac{1}{R^{d-1}} \asymp k^{1-1/d}$, which implies the rate $O(h^2) + O_p\left(\sqrt{\frac{k^{1-1/d}}{nh}}\right) + O_p\left(\frac{1}{nh^3}\right)$. Under our reference rule $k = \sqrt{n}$ the optimal bandwidth is $h \asymp n^{-\frac{1}{10}(1+\frac{1}{d})}$. Recall that the local sample size is about $n_{loc} = n/k = \sqrt{n}$ and hence the optimal bandwidth is $h \asymp n_{loc}^{-\frac{1}{5}(1+\frac{1}{d})}$. When $d \rightarrow \infty$, this leads to $h \asymp n_{loc}^{-1/5}$, which is the same rate on sample size as given by the Silverman’s rule of thumb.

5 Simulations

The above theoretical analysis justifies the reliability of the density-based weights proposed for skeleton clustering. To study the effectiveness of skeleton clustering as

a clustering method, we conduct several Monte Carlo experiments. In particular, we present empirical results to illustrate (1) the performance of skeleton clustering in multivariate and high-dimensional settings, (2) the robustness of skeleton clustering to noises, and (3) the ability to deal with overlapping clusters. We include several additional simulations to show the effectiveness of skeleton clustering in Appendix C.

5.1 High-dimensional Setting

In this section, we present the performance of skeleton clustering using 3 simulated datasets: the Yinyang data, the Mickey data, and the Manifold Mixture data. We also include an additional simulation called Ring data in Appendix C.4.

In the following sections, when using the skeleton clustering methods, the number of knots is set to be $k = \lceil \sqrt{n} \rceil$, the knots are chosen by k -means, and we use single linkage hierarchical clustering when merging knots into final clusters. We select smoothing bandwidth by Silverman’s rule of thumb for the FD and TD, and the radius of TD is set to be the same for all edges with the value chosen as the average within Voronoi cells variance. To highlight the importance of density-based similarity measures, we include a similarity measure called average distance (AD) for comparison. AD measures the similarity between c_j and c_ℓ using the inverse of the average distances between all pairs of observations in the two corresponding Voronoi cells. All simulations are repeated 100 times to obtain the distribution of the empirical performance.

5.1.1 Yinyang Data

The Yinyang dataset is an intrinsically 2-dimensional data containing 5 components: a big outer circle with 2000 data points, two inner semi-circles each with 200 data points, and two clumps each with 200 data points. The total sample size is $n = 3200$ and according to our reference rule we choose $k = \lceil \sqrt{3200} \rceil = 57$ knots for the skeleton clustering procedure. To make the data high-dimensional, we include additional variables from a Gaussian noise with mean 0 and standard deviation 0.1, and we increase the dimension of noise variables so that the total dimensions are $d = 10, 100, 500, 1000$. We empirically compare the following clustering approaches: direct single-linkage hierarchical clustering (SL), direct k -means clustering (KM), spectral clustering (SC), skeleton clustering with average distance density

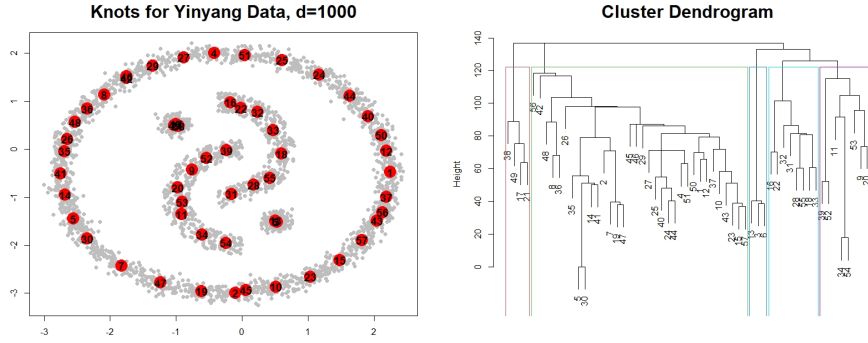


Figure 8: Knots chosen by k -means on Yinyang data and the Dendrogram for single linkage hierarchical clustering with similarity measured by Voronoi density.

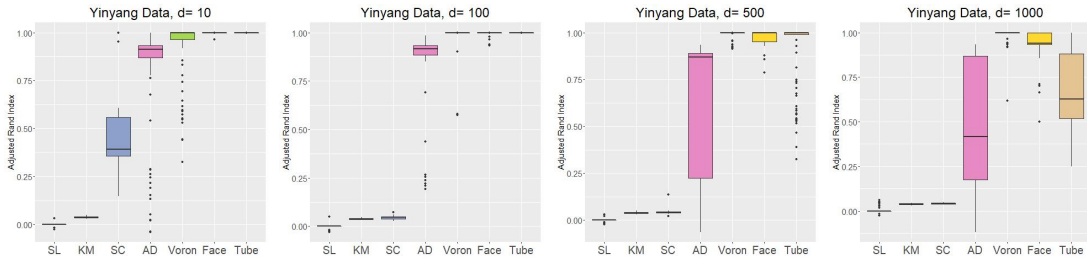


Figure 9: Comparison of the final clustering performance in terms of adjusted Rand Index with different clustering methods on Yinyang Data with dimension 10, 100, 500, and 1000.

(AD), skeleton clustering with Voronoi density (Voron), skeleton clustering with Face density (Face), and skeleton clustering with Tube density (Tube). Since this is a simulated data, we know that there are exactly 5 clusters and we know which cluster an observation belongs to. We use the Adjusted Rand Index (Rand, 1971; Hubert and Arabie, 1985) to measure the performance of each clustering method.

The results are given in Figure 9. We observe that when dimension increases, traditional methods (SL, KM, SC) fail to give good clustering results while skeleton clustering can generate nearly perfect clustering. Across all the data dimensions, the Voronoi density, the simplest measure among the three proposed similarity measures, gives the best performance in skeleton clustering framework. Face density and Tube density both have satisfying performance. Average distance density becomes problematic in high-dimensional settings but still gives significantly better performance than directly applying single-linkage hierarchical clustering or spectral clustering. The fact that all skeleton clustering methods perform better than the traditional methods highlights the effectiveness of using the skeleton clustering framework. Moreover, all three density-based similarity measures outperform the average distance, which illustrates the power of using density-based weights in clustering.

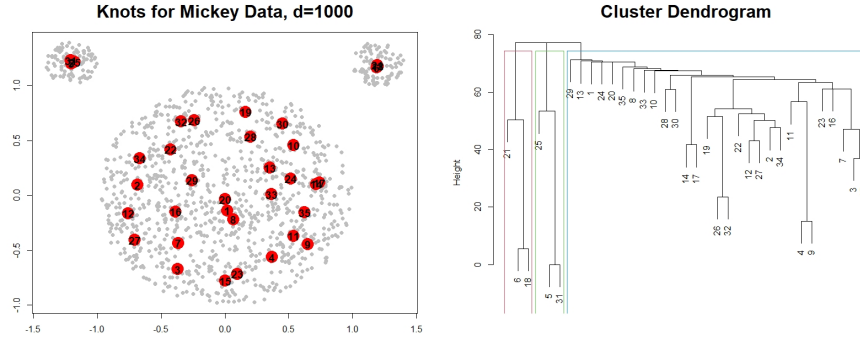


Figure 10: An illustration of the analysis of the Mickey data with dimension 100.

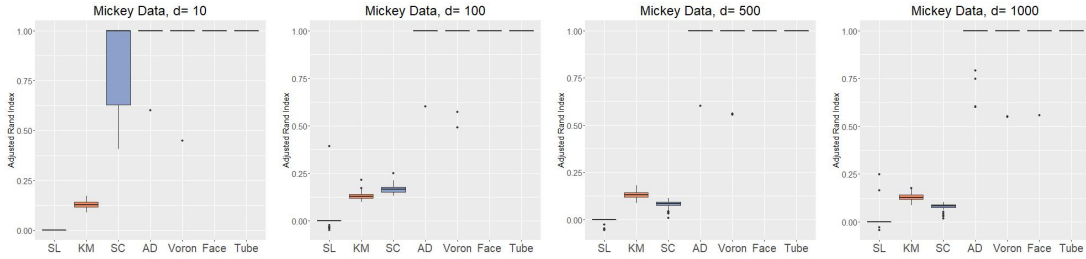


Figure 11: Comparison of adjusted Rand index using different similarity measures on Mickey data with dimensions 10, 100, 500, 1000.

5.1.2 Mickey Data

The simulated Mickey data is an intrinsically 2-dimensional data consists of one large circular region with 1000 data points and two small circular regions each with 100 data points. As a result, the structures have unbalanced sizes. The total sample size is $n = 1200$ and we choose the number of knots to be $k = \lceil \sqrt{1200} \rceil = 35$. We include additional variables with random Gaussian noises to make it a high dimensional data ($d = 10, 100, 500, 1000$) the same way as in Section 5.1.1. The left panel of Figure 10 shows the scatter plot of the first two dimensions.

We perform the same comparisons as done on the Yinyang data in Section 5.1.1, and the results are displayed in Figure 11. All methods perform well when d is small but starting at $d = 100$, traditional methods fail to recover the underlying clusters. On the other hand, all methods in the skeleton clustering framework work well even when $d = 1000$.

5.1.3 Manifold Mixture Data

In the previous two experiments, the underlying components are all two-dimensional structures. Here we consider data composed of structures of different intrinsic dimensions, and we call it the manifold mixture data. The simulated manifold mixture

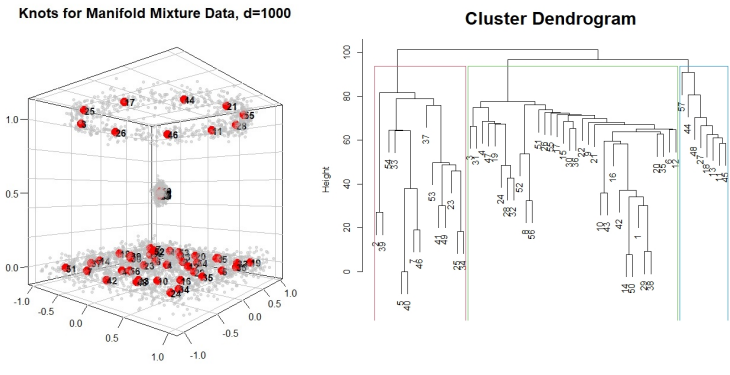


Figure 12: Results on Manifold Mixture data with dimension 100.

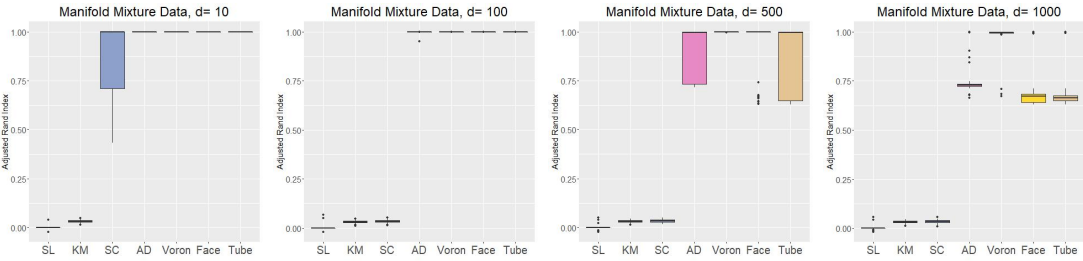


Figure 13: Comparison of adjusted Rand index using different similarity measures on Manifold Mixture data with dimensions 10, 100, 500, 1000

data, as illustrated in the left panel of Figure 12, consists of a 2-dimensional plane with 2000 data points, a 3-dimensional Gaussian cluster with 400 data points, and an essentially 1-dimensional ring shape with 800 data points. There are a total of 3200 observations and we choose $k = \lceil \sqrt{3200} \rceil = 57$ knots. Similar to the other two simulations, we include Gaussian noise variables to make the data high-dimensional ($d = 10, 100, 500, 1000$) and make comparisons between the same set of clustering methods.

Figure 13 summarizes the performance of each method. Traditional methods (SL, KM, and SC) do not perform well when $d > 10$ while all methods of skeleton clustering perform very well when $d \leq 500$. Notably, the skeleton clustering with VD still has a perfect performance even when $d = 1000$, whereas skeleton clustering based on other similarity measures gives satisfying results.

5.2 Data with Noise

In this section, we assess the performance of skeleton clustering on data with additive noises. We added 640 (20% of the true signals) noisy points to the Yinyang dataset ($d = 1000$) used in Section 5.1.1. The noisy points are sampled uniformly in the first two dimensions, and we include the random Gaussian noises in the other 998

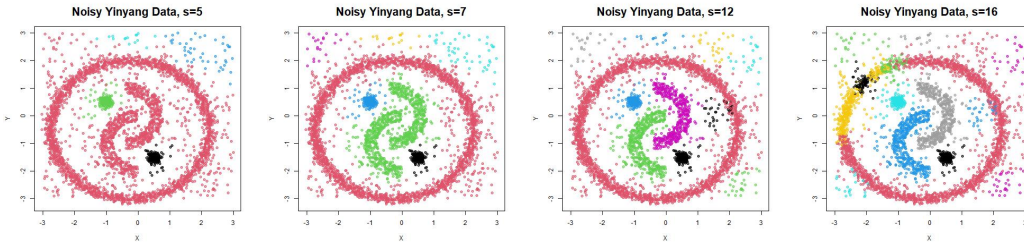


Figure 14: The final clustering result with single linkage hierarchical clustering for Yinyang data with noise, $d = 1000$.

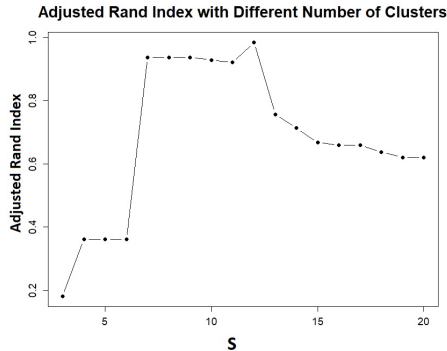


Figure 15: Adjusted Rand Index with different number of final clusters S .

variables the same way we generated Yinyang data. We apply the overfitting k -means to construct $k = \lceil \sqrt{3840} \rceil = 62$ knots. We use Voronoi density to measure the edge weights and apply single linkage hierarchical clustering to segment the knots into S final clusters. For this experiment we let S to take on different values.

Figure 14 summarizes the results. In the first panel, one can see that the original choice $S = 5$ does not provide a good clustering result due to the added noises. However, when S gets larger, we start to identify more structures. When $S = 12$, we are able to recover the original five components. When S gets too large, like in the last panel with $S = 16$, we would partition the original structure into many small pieces. In fact, our experiment shows that when the number of final clusters S is between 7 and 12, we are able to reliably recover the main components with high adjusted Rand Index (Figure 15). Thus, this experiment shows that the skeleton clustering is robust to the added noise, but we may need to increase the final number of clusters S to account for the noise.

5.3 Overlapping Clusters

It is known that when the components are not well-separated with some degree of overlapping, hierarchical clustering with single linkage will fail to detect the underly-

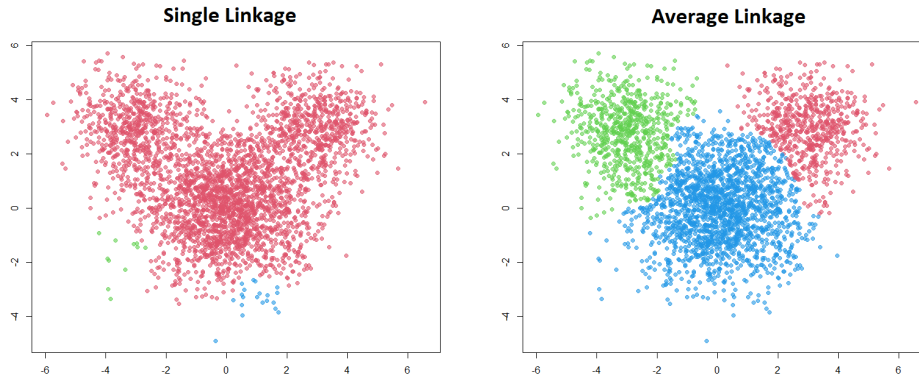


Figure 16: Clustering result with single-linkage (left) and average-linkage (right) as the segmentation rule.

ing structure. By using single linkage in the knots segmentation step, we may suffer from the same issue. Such an example is given in section and a possible way to deal with overlapping clusters is presented.

In this experiment, we consider a three-Gaussian mixture model in 2D case that we call it the Mix Mickey data. The covariance matrices of the three clusters are all diagonal with 2 on the diagonal entries. The center of the large cluster is at $(0, 0)$ and has 2000 sample points. The two smaller clusters are centered at $(3, 3)$ and $(-3, 3)$ respectively and each has 600 sample points. As can be seen in Figure 16, the three clusters have a substantial amount of overlapping so that it is difficult for clustering methods to separate them into three distinct clusters.

We use the same analysis pipeline as in Section 5.1.2 except that we consider only the Voronoi density because it always performs the best. In the left panel of Figure 16, when we perform knots segmentation with the single linkage criterion, we are unable to detect the three structures. Even if we increase the total number of final clusters, we either fail to discover the true three clusters or fragment the components into too many small pieces. However, using the average linkage instead, we are able to recover the underlying three components (right panel of Figure 16). The main reason is that the average linkage is a criterion that tends to create spherical clusters with similar sizes. Thus, our experiment shows that if data contains overlapping clusters and we know the clusters are roughly spherical, then we can use the average linkage criterion in the knots segmentation step to accommodate for the overlaps.

For comprehensiveness, we also tested the performance of other popular linkage criteria in Appendix C.5, but only the average linkage has a reliable performance in detecting overlapping clusters. In sum, the simulations in this section demonstrate

that the skeleton clustering framework is powerful in detecting clusters with various shapes for high-dimensional data and is flexible with noisy data and overlapping clusters.

6 Real Data

In this section, we apply skeleton clustering to two real data examples: Zipcode data and GvHD data. We also analyze the Olive Oil data in Appendix C.6.

6.1 Zipcode Data

This dataset consists of $n = 2000$ 16×16 images of handwritten Hindu-Arabic numerals from (Stuetzle and Nugent, 2010). We use the overfitting k -means to find $k = 45$ knots. Similar to the procedure in Section 5.1, we consider four similarity measures to obtain the edge weight: VD, FD, TD, and AD. We compare the performance of the four skeleton clustering approaches to three traditional methods: the direct single linkage hierarchical clustering (SL), the direct k -means clustering (KM), and spectral clustering (SC). We use the single linkage as the criterion to segment knots.

The result is shown in the left panel of Figure 17 with the adjusted Rand index plotted against different number of total cluster S . The gray vertical line indicates the choice of $S = 10$, which is the actual number of clusters. The skeleton clustering with VD (Voron) gives the best clustering result in terms of adjusted Rand index at the true 10 clusters and gives good clustering results when the number of clusters is specified to be larger than the truth. However we note that spectral clustering (SC) and naive k -means clustering (KM) give comparably good results with small number of clusters.

The right panel of Figure 17 is the “denoised” version of the digits. We estimate the density of each observation by \sqrt{n} -NN density estimator and remove the observations with the lowest 10% density. We see that all clustering results are slightly improved, but such improvement may come from the decreased total sample size after denoising. Notably, the skeleton clustering with Tube density (Tube) generates significantly better clustering results after denoising the data, giving adjusted Rand indexes comparable to skeleton clustering with Voronoi density. This shows skeleton clustering with Tube density can be sensitive to noises in real data but still has the



Figure 17: Comparison of different similarity measures on all Zipcode Data.

potential to give insightful clustering results.

6.2 GvHD Data

In this section, we consider a famous flow cytometry data from (Brinkman et al., 2007) known as the graft-versus-host disease (GvHD) data. GvHD is a significant problem in the field of allogeneic blood and marrow transplantation which occurs when allogeneic hematopoietic stem cell transplant recipients when donor-immune cells in the graft attack the tissues of the recipient. The data include samples from a patient with GvHD containing $n_1 = 9083$ observations and samples from a control patient with $n_2 = 6809$ observations. Both samples include four biomarker variables, CD4, CD8 β , CD3, and CD8. Previous studies (Brinkman et al., 2007; Lo et al., 2008; Baudry et al., 2010) have identified the presence of high values of CD3, CD4, CD8 β cell sub-populations as a significant characteristic in the GvHD positive sample. Thus, we focus on these three variables (CD3, CD4, CD8 β) for plotting but we still use all four biomarker variables in our clustering analysis. We apply the proposed skeleton clustering to analyze this dataset. In addition to meaningful clustering result, later we will show that our skeleton clustering procedure may also lead to a novel two-sample test.

The two samples are plotted in the left panel of Figure 18 with blue points from the control sample and the red points from the GvHD positive sample. We observe that, in addition to the presence of observations in the high CD3, CD4, CD8 β region, the distribution of the positive sample is also different from the control sample in the region with medium to the low CD3, CD4, and CD8 β . Later we will demonstrate that our clustering framework can identify all such differences in distributions.

To apply the skeleton clustering to make fair comparisons for the two samples, we first construct knots from each sample respectively. In more details, we apply the

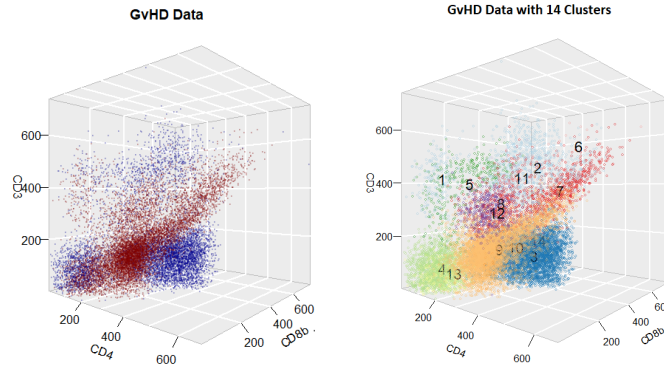


Figure 18: **Left:** 3D scatterplot of the positive sample (red) and the control sample (blue). **Right:** Final clustering result of combined GvHD data.

k -means method to find $k_1 = \lceil \sqrt{n_1} \rceil$ knots for the positive sample and find $k_2 = \lceil \sqrt{n_2} \rceil$ knots for the control sample. This ensure that both sample are well-represented by knots. We then combine the two samples into one dataset and combine the knots for each sample into one set with $k_1 + k_2$ combined knots. We create edges among the combined knots and apply the Voronoi density (VD) to measure the edge weights since VD always performs the best in our simulations. To segment the knots, we use average linkage criterion because the scatterplot in the left panel of Figure 18 shows that the clusters can be overlapping and the analysis in Section 5.3 suggests to use average linkage to deal with overlapping clusters. The skeleton clustering result is displayed in the right panel of Figure 18 with the number of final cluster chosen to be $S = 14$ as suggested by (Baudry et al., 2010). Our clustering result captures the cluster structure of the combined data.

For further insights, we examined the weighted proportion of positive observations in each cluster. The proportionally smaller weight is assigned to each positive observation to accommodate the fact that more positive observations ($n_1 = 9083 \neq n_2 = 6809$) are presented in the combined data. Consequently, a weighted proportion of 0.5 means that the two samples are balanced in one region.

A summary of the weighted proportion of clusters is presented in Table 1. We note that clusters 7,9,12, and 13 are majorly composed of positive observations (proportion > 0.75), and clusters 3 and 6 are majorly composed of observations from the control sample (proportion < 0.25). We also include the p-value for testing if the the proportions equal 0.5. Admittedly, because we use the data to find clusters and use the same data again to do the test, the p-values in Table 1 may tend to be small.

Clusters with majorly positive observations and clusters with majorly control

Cluster	1	2	3	4	5	6	7
Size	202	948	3881	1859	338	17	812
Prop	.458	.343	.008	.296	.341	.000	.934
p-value	.30	7×10^{-20}	0	3×10^{-63}	4×10^{-8}	1×10^{-4}	6×10^{-103}
Cluster	8	9	10	11	12	13	14
Size	468	6191	251	37	478	402	8
Prop	.690	.888	.673	.669	.794	.841	.310
p-value	2×10^{-13}	0	1×10^{-6}	.09	6×10^{-30}	3×10^{-33}	.52

Table 1: Table of the sizes of the clusters and the weighted proportion of positive observations within each cluster. A proportion 0.5 indicates that the two sample has equal proportion in the region. The p -value is the simple proportional test to examine if the two sample has equal proportion in that cluster.

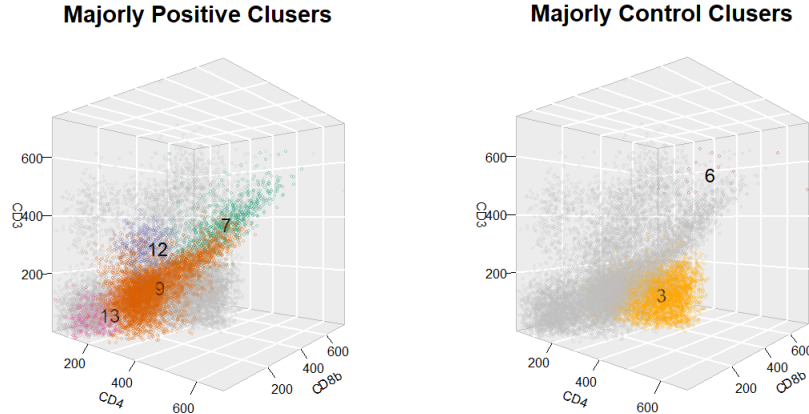


Figure 19: Clusters with majorly positive observations and majorly control observations

observations are depicted in the two panels in Figure 19. Cluster 7 corresponds to the high CD3, CD4, CD8 β region as identified in Brinkman et al. (2007); Baudry et al. (2010). Moreover, we identify new regions with high proportion of positive samples: cluster 9, 12, and 13. These clusters are in mid to low CD3, CD4, CD8 β region, which is different from what was identified in Brinkman et al. (2007); Baudry et al. (2010). For the control case, we identify two major clusters: cluster 3 and 6. Cluster 3 is a large cluster with nearly all the observations are from the control sample. It is located in the high CD8 β but low CD3 and CD4 region. Cluster 6 is scattered in the high CD3, CD4, CD8 β region, a region known to be associated with positive sample. However, this cluster has a small size (only 17 cells), so it is unclear if it is a real structure or due to purely randomness.

Our results suggest a future procedure for diagnosing GvHD. Biomarkers from a new patient can be divided into clusters with respect to the learnt segmentation, and doctors can mainly focus on the sample points that fall into region 3, 7, 9, 12, and 13. If the patient has many points in cluster 7, 9, 12, and 13, it is likely that the patient has GvHD. Note that our current result is only based on two individuals; to use

it for practical diagnosis, we need to find clusters based on a large and representative population.

7 Conclusion

In this work, we introduced the skeleton clustering framework that can handle multivariate and high-dimensional clustering problems with complex cluster shapes. Our method allows the use of density-based clustering to the high dimensional regime. The key to bypass the curse of dimensionality is the use of density surrogate such as Voronoi density, Face density, and Tube density that are less sensitive to the dimension. We use both theoretical and empirical analysis to illustrate the effectiveness of the skeleton clustering procedure.

In what follows, we describe some possible future directions:

- **Skeleton clustering with similarity matrix.** The idea of skeleton clustering may be generalized to data where we only observe the similarity/distance matrices such as network data. Knots can be restricted to indices in the data and we choose them by minimizing the k -means criterion. While face and tube density cannot be computed, the Voronoi density is still applicable since we only need the information about pairs of observations. This might provide a new approach for community detection in network data ([Lancichinetti and Fortunato, 2009](#); [Zhao, 2017](#); [Abbe, 2017](#)).
- **Accounting for the randomness of knots.** For our current theoretical analysis, we assume that the knots are given and non-random. But in practice, knots are computed from the data as well. There are two technical challenges when dealing with random knots. First, the randomness of knots may be correlated with the randomness of estimated edge weight, so the calculation of rates is much more complicated. Second, while there are established theories for k -means algorithm ([Graf and Luschgy, 2000, 2002](#); [Hartigan and Wong, 1979](#)), these results only apply to the global minimum of the objective function. In reality, we are unlikely to obtain the global minimum but instead, our inference is based on a local minimum. It is unclear how to properly derive a theoretical statement based on local minima, so we leave this as future work.
- **Detecting boundary points between clusters.** Our skeleton clustering

method can be applied to detect points on the boundary between two clusters. The idea is simple—in the final cluster assignment, instead of assigning only one label to an observation, we assign H labels to an observation based on the cluster labels of H -nearest knots. The homogeneity of the label assignment can be used as a quantity to detect if a point is on the boundary or in the interior of a cluster and may serve as an uncertainty quantification of clustering. We will pursue this in the future.

References

- E. Abbe. Community detection and stochastic block models: recent developments. *The Journal of Machine Learning Research*, 18(1):6446–6531, 2017.
- N. Amenta, D. Attali, and O. Devillers. Complexity of delaunay triangulation for points on lower-dimensional polyhedra. In *Proceedings of the Eighteenth Annual ACM-SIAM Symposium on Discrete Algorithms, SODA '07*, pages 1106–1113, USA, 2007. Society for Industrial and Applied Mathematics. ISBN 9780898716245.
- A. Azzalini and N. Torelli. Clustering via nonparametric density estimation. *Statistics and Computing*, 17(1):71–80, 2007.
- O. Bachem, M. Lucic, and A. Krause. Practical coresets constructions for machine learning, 2017.
- J.-P. Baudry, A. E. Raftery, G. Celeux, K. Lo, and R. Gottardo. Combining mixture components for clustering. *Journal of Computational and Graphical Statistics*, 19(2):332–353, 2010. doi: 10.1198/jcgs.2010.08111.
- J. L. Bentley. Multidimensional binary search trees used for associative searching. *Commun. ACM*, 18(9):509–517, Sept. 1975. ISSN 0001-0782. doi: 10.1145/361002.361007. URL <https://doi.org/10.1145/361002.361007>.
- A. W. Bowman. An alternative method of cross-validation for the smoothing of density estimates. *Biometrika*, 71(2):353–360, 1984. ISSN 00063444.
- R. R. Brinkman, M. Gasparetto, S. J. J. Lee, A. J. Ribickas, J. Perkins, W. Janssen, R. Smiley, and C. Smith. High-Content Flow Cytometry and Temporal Data Analysis for Defining a Cellular Signature of Graft-Versus-Host Disease. *Biology of Blood and Marrow Transplantation*, 13(6):691–700, jun 2007. ISSN 10838791. doi: 10.1016/j.bbmt.2007.02.002.
- M. A. Carreira-Perpinán. A review of mean-shift algorithms for clustering. *arXiv preprint arXiv:1503.00687*, 2015.
- J. E. Chacón. A Population Background for Nonparametric Density-Based Clustering. *Statistical Science*, 30(4):518–532, 2015. doi: 10.1214/15-STS526.
- J. E. Chacón and T. Duong. Data-driven density derivative estimation, with applications to nonparametric clustering and bump hunting. *Electronic Journal of Statistics*, 7:499–532, 2013.
- J. E. Chacón, T. Duong, and M. P. Wand. Asymptotics for General Multivariate Kernel Density Derivative Estimators. *Statistica Sinica*, 21(2):807–840, 2011.
- K. Chaudhuri and S. Dasgupta. Rates of convergence for the cluster tree. In *Proceedings of the 23rd International Conference on Neural Information Processing Systems - Volume 1, NIPS'10*, pages 343–351, Red Hook, NY, USA, 2010. Curran Associates Inc.

- K. Chaudhuri, S. Dasgupta, S. Kpotufe, and U. von Luxburg. Consistent procedures for cluster tree estimation and pruning. *IEEE Transactions on Information Theory*, 60(12):7900–7912, 2014.
- B. Chazelle. An optimal convex hull algorithm in any fixed dimension. *Discrete & Computational Geometry*, 10(1):377–409, dec 1993. ISSN 01795376. doi: 10.1007/BF02573985. URL <https://link.springer.com/article/10.1007/BF02573985>.
- Y.-C. Chen. A Tutorial on Kernel Density Estimation and Recent Advances. *Bio-statistics and Epidemiology*, 1(1):161–187, apr 2017.
- Y. C. Chen, C. R. Genovese, and L. Wasserman. A comprehensive approach to mode clustering. *Electronic Journal of Statistics*, 10(1):210–241, 2016. ISSN 19357524. doi: 10.1214/15-EJS1102.
- Y. Cheng. Mean shift, mode seeking, and clustering. *IEEE transactions on pattern analysis and machine intelligence*, 17(8):790–799, 1995.
- A. Cuevas, M. Febrero, and R. Fraiman. Estimating the number of clusters. *Canadian Journal of Statistics*, 28(2):367–382, 2000.
- A. Cuevas, M. Febrero, and R. Fraiman. Cluster analysis: A further approach based on density estimation. *Computational Statistics and Data Analysis*, 36(4):441–459, 2001. ISSN 01679473. doi: 10.1016/S0167-9473(00)00052-9.
- B. Delaunay. Sur la sphère vide. a la mémoire de georges voronoï. *Bulletin de l'Académie des Sciences de l'URSS. Classe des sciences mathématiques et na*, 6: 793–800, 1934.
- J. Eldridge, M. Belkin, and Y. Wang. Beyond hartigan consistency: Merge distortion metric for hierarchical clustering. volume 40 of *Proceedings of Machine Learning Research*, pages 588–606, Paris, France, 03–06 Jul 2015. PMLR.
- M. Ester, H.-P. Kriegel, J. Sander, and X. Xu. A density-based algorithm for discovering clusters in large spatial databases with noise. In *Proceedings of the Second International Conference on Knowledge Discovery and Data Mining, KDD'96*, pages 226–231. AAAI Press, 1996.
- C. Fraley and A. E. Raftery. Model-based clustering, discriminant analysis, and density estimation. *Journal of the American Statistical Association*, 97(458):611–631, 2002. ISSN 01621459. doi: 10.1198/016214502760047131.
- A. L. N. Fred and A. K. Jain. Combining multiple clusterings using evidence accumulation. *IEEE Transactions on Pattern Analysis and Machine Intelligence*, 27(6):835–850, 2005. doi: 10.1109/TPAMI.2005.113.
- K. Fukunaga and L. Hostetler. The estimation of the gradient of a density function, with applications in pattern recognition. *IEEE Transactions on information theory*, 21(1):32–40, 1975.
- A. D. Gordon. A Review of Hierarchical Classification. *Journal of the Royal Statistical Society. Series A (General)*, 150(2):119, mar 1987. ISSN 00359238. doi: 10.2307/2981629.
- S. Graf and H. Luschgy. *Foundations of Quantization for Probability Distributions*, volume 1730 of *Lecture Notes in Mathematics*. Springer Berlin Heidelberg, Berlin, Heidelberg, 2000. ISBN 978-3-540-67394-1. doi: 10.1007/BFb0103945.
- S. Graf and H. Luschgy. Rates of Convergence for The Empirical Quantization Error. 30(2):874–897, 2002.
- J. A. Hartigan and M. A. Wong. Algorithm AS 136: A K-Means Clustering Algorithm. *Applied Statistics*, 28(1):100, 1979. ISSN 00359254. doi: 10.2307/2346830.

- T. Heskes. Self-organizing maps, vector quantization, and mixture modeling. *IEEE Transactions on Neural Networks*, 12(6):1299–1305, 2001.
- L. Hubert and P. Arabie. Comparing partitions. *Journal of Classification*, 2(1):193–218, dec 1985. ISSN 01764268. doi: 10.1007/BF01908075.
- J. Kim, Y.-C. Chen, S. Balakrishnan, A. Rinaldo, and L. Wasserman. Statistical inference for cluster trees. In D. D. Lee, M. Sugiyama, U. V. Luxburg, I. Guyon, and R. Garnett, editors, *Advances in Neural Information Processing Systems 29*, pages 1839–1847. Curran Associates, Inc., 2016.
- J. S. Klemelä. *Smoothing of multivariate data: density estimation and visualization*, volume 737. John Wiley & Sons, 2009.
- G. N. Lance and W. T. Williams. A General Theory of Classificatory Sorting Strategies: 1. Hierarchical Systems. *The Computer Journal*, 9(4):373–380, feb 1967. ISSN 0010-4620. doi: 10.1093/comjnl/9.4.373.
- A. Lancichinetti and S. Fortunato. Community detection algorithms: a comparative analysis. *Physical review E*, 80(5):056117, 2009.
- J. Li, S. Ray, and B. G. Lindsay. A nonparametric statistical approach to clustering via mode identification. *Journal of Machine Learning Research*, 8(8), 2007.
- S. P. Lloyd. Least Squares Quantization in PCM. *IEEE Transactions on Information Theory*, 28(2):129–137, 1982. ISSN 15579654. doi: 10.1109/TIT.1982.1056489.
- K. Lo, R. R. Brinkman, and R. Gottardo. Automated gating of flow cytometry data via robust model-based clustering. In *Cytometry Part A*, volume 73, pages 321–332. Cytometry A, apr 2008. doi: 10.1002/cyto.a.20531.
- R. Maitra. Initializing partition-optimization algorithms. *IEEE/ACM Transactions on Computational Biology and Bioinformatics*, 6(1):144–157, 2009. doi: 10.1109/TCBB.2007.70244.
- D. M. Mason, W. Polonik, et al. Asymptotic normality of plug-in level set estimates. *The Annals of Applied Probability*, 19(3):1108–1142, 2009.
- G. Menardi and A. Azzalini. An advancement in clustering via nonparametric density estimation. *Statistics and Computing*, 24(5):753–767, 2014.
- F. Murtagh. A Survey of Recent Advances in Hierarchical Clustering Algorithms. *The Computer Journal*, 26(4):354–359, nov 1983. ISSN 0010-4620. doi: 10.1093/comjnl/26.4.354.
- R. Nugent and W. Stuetzle. Clustering with confidence: A low-dimensional binning approach. In *Classification as a Tool for Research*, pages 117–125. Springer, 2010.
- A. D. Peterson, A. P. Ghosh, and R. Maitra. Merging k-means with hierarchical clustering for identifying general-shaped groups. *Stat*, 7(1):e172, 2018.
- D. Pollard. A Central Limit Theorem for k-Means Clustering. *The Annals of Probability*, 10(4):919–926, 1982.
- W. M. Rand. Objective Criteria for the Evaluation of Clustering Methods. *Journal of the American Statistical Association*, 66(336):846, dec 1971. ISSN 01621459. doi: 10.2307/2284239.
- A. Rinaldo, A. Singh, R. Nugent, and L. Wasserman. Stability of density-based clustering. *Journal of Machine Learning Research*, 13:905, 2012.
- M. Rudemo. Empirical choice of histograms and kernel density estimators. *Scandinavian Journal of Statistics*, 9:65–78, 1982.

- D. W. Scott. *Multivariate density estimation: theory, practice, and visualization*. John Wiley & Sons, 2015.
- B. W. Silverman. *Density estimation for statistics and data analysis*, volume 26. CRC press, 1986.
- W. Stuetzle and R. Nugent. A generalized single linkage method for estimating the cluster tree of a density. *Journal of Computational and Graphical Statistics*, 19(2): 397–418, 2010. ISSN 10618600. URL <http://www.jstor.org/stable/25703575>.
- R. Tibshirani, G. Walther, and T. Hastie. Estimating the number of clusters in a data set via the gap statistic. *Journal of the Royal Statistical Society. Series B: Statistical Methodology*, 63(2):411–423, jan 2001. ISSN 13697412. doi: 10.1111/1467-9868.00293.
- M. Tsimidou, R. Macrae, and I. Wilson. Authentication of virgin olive oils using principal component analysis of triglyceride and fatty acid profiles: Part 1—classification of greek olive oils. *Food Chemistry*, 25(3):227 – 239, 1987. ISSN 0308-8146.
- G. Voronoi. Recherches sur les paralléloèdres primitives. *J. reine angew. Math*, 134: 198–287, 1908.
- M. P. Wand and M. C. Jones. Multivariate plug-in bandwidth selection. *Computational Statistics*, 9(2):97–116, 1994.
- L. Wasserman. *All of Nonparametric Statistics*. Springer New York, 2006. doi: 10.1007/0-387-30623-4.
- R. Weber, H.-J. Schek, and S. Blott. A quantitative analysis and performance study for similarity-search methods in high-dimensional spaces. In *Proceedings of the 24rd International Conference on Very Large Data Bases, VLDB '98*, pages 194–205, San Francisco, CA, USA, 1998. Morgan Kaufmann Publishers Inc. ISBN 1558605665.
- Y. Zhao. A survey on theoretical advances of community detection in networks. *Wiley Interdisciplinary Reviews: Computational Statistics*, 9(5):e1403, 2017.

Appendices

A Computational Complexity

Knots construction. The first step of skeleton clustering is choosing knots, and in this work we take overfitting k -means as the default method. The k -means algorithm of Hartigan and Wong ([Hartigan and Wong, 1979](#)) has time complexity $O(ndkI)$, where n is the number of points, d is the dimension of the data, k is the number of clusters for k -means, and I is the number of iterations needed for convergence. When using overfitting k -means to chooses knots, the reference rule is $k = \sqrt{n}$, and hence the complexity is $O(n^{3/2}dI)$. This is a time consuming step of our clustering framework, and the complexity increases linearly with d . Therefore, preprocessing the data with dimension reduction techniques or using subject knowledge to choose knots can be helpful to speed up this process.

Edges construction. For the edge construction step, we approximate the Delaunay Triangulation with $\widehat{DT}(\mathcal{C})$ by looking at the 2-NN neighborhoods (the Voronoi Density regions in 3.1). Hence the main computational task for our edge construction step is the 2-nearest knot search. We used the k-d tree algorithm for this purpose, which gives the worst-case complexity of $O(ndk^{(1-1/d)})$. Notably, the computation complexity at this step is at the worst linear in d , which is a much better rate than computing the exact Delaunay Triangulation (exponential dependence on d), and our empirical studies have illustrated the effectiveness of such approximation.

Edge weight construction: VD. Next, we consider the computation complexity of the different edge weights measurements. For the VD, its numerator can be computed directly from the 2-NN search when constructing the edges and hence no additional computation is needed. The denominators are pairwise distances between knots and can be computed with the worst-case complexity of $O(dk^2)$ because the number of nonzero edges is less than $\frac{k(k-1)}{2}$. With $k = \sqrt{n}$, we have the total time complexity of computing the VD to be $O(nd)$.

Edge weight construction: FD. For the Face density, we calculate the projected KDE at the middle point for each pair of neighboring Voronoi cells. The projection of one data point onto one central line can be done by matrix multiplication with complexity $O(d)$. Recall that we only use data points in local Voronoi cells for FD calculation, and the local sample size would be at $n_{loc} = O(\sqrt{n})$ under the conditions in Section 4 and the reference rule $k = \lceil \sqrt{n} \rceil$. Together it takes $O(d\sqrt{n})$ to calculate the projected data for one edge. With the projected data, KDE calculation has a time complexity $O(c \log c)$ where $c = \max_{j \neq \ell} \{n_j + n_\ell\}$ for any pair of knot indexes j, ℓ . Again we have $c = O(n/k) = O(\sqrt{n})$ under the previously mentioned conditions. We need to do KDE for each edge in the skeleton, which gives the overall time complexity of FD weights to $O(k^2 d \sqrt{n} + k^2 c \log c) = O(n^{3/2} d + n^{3/2} \log n)$.

Edge weight construction: TD. For Tube density, we similarly perform a projected KDE for each edge. Let η be the maximum number of points in a tube region $\eta = \max_{j, \ell} |\{X_i : \|\Pi_{j\ell}(X_i) - X_i\| \leq R\}|$, the data projection again takes $O(\eta d)$ complexity. Suppose the minimum density is obtained by a grid search with m grid points, the KDE step takes a total of $O(m\eta \log \eta)$ for one edge. To compute the whole edge weights matrix with $k = \sqrt{n}$, we have the complexity to be $O(n\eta d + nm\eta \log \eta)$. Under conditions where the tube regions for TD estimations is also of size $\eta = O(n/k) = O(\sqrt{k})$, we have the overall complexity for VD weights calculation

to be $O(k^2 d \sqrt{n} + k^2 c \log c) = O(n^{3/2} d + mn^{3/2} \log n)$, which is larger than that for FD due to the grid search for minimum density.

Knots segmentation. In this work, we segment the learned weighted skeleton using hierarchical clustering. With links that can be updated by Lance-Williams update (Lance and Williams, 1967) and satisfies the reducibility condition (Gordon, 1987), hierarchical clustering can be carried out with computation complexity $O(N^2)$, where N is the number of points to start the algorithm with (Murtagh, 1983). For our empirical results we favored single linkage and average linkage, and both satisfy the requirements for efficient hierarchical clustering algorithm. We perform hierarchical clustering on the $k = \sqrt{n}$ knots, and hence the computation complexity for segmenting the skeleton structure is $O(k^2) = O(n)$.

B Proof

B.1 Voronoi Density

We restate the assumption:

- (B1) There exists a constant c_0 such that the minimal knot size $\min_{(j,\ell) \in E} \mathbb{P}(A_{j\ell}) \geq \frac{c_0}{k}$ and $\min_{(j,\ell) \in E} \|c_j - c_\ell\| \geq \frac{c_0}{k^{1/d}}$.

PROOF OF THEOREM 1. For given knots c_j, c_ℓ , the distance $\|c_j - c_\ell\|$ is also given. We denote the numerator of $S_{j\ell}^{VD}$ as

$$p_{j\ell} = \mathbb{P}(A_{j\ell}) = \mathbb{E}I(X_i : d(X_i, c_m) > \max\{d(X_i, c_j), d(X_i, c_\ell), \forall m \neq j, l\})$$

and note that the numerator of $\widehat{S}_{j\ell}^{VD}$ is

$$\widehat{P}_n(A_{j\ell}) = \frac{1}{n} \sum_{i=1}^n I(X_i : d(X_i, c_m) > \max\{d(X_i, c_j), d(X_i, c_\ell), \forall m \neq j, l\}),$$

which is a sum of binary variables and has variance $\sigma_{j\ell}^2 = \frac{p_{j\ell}(1-p_{j\ell})}{n}$. By the Chebyshev's inequality,

$$|\widehat{P}_n(A_{j\ell}) - p_{j\ell}| = O_p(\sigma_{j\ell}^{1/2}) = O_p\left(\left[\frac{p_{j\ell}(1-p_{j\ell})}{n}\right]^{1/2}\right)$$

Note that the region $A_{j\ell}$ is changing with respect to k . The ratio is then

$$\begin{aligned} \left| \frac{\widehat{S}_{j\ell}^{VD}}{S_{j\ell}^{VD}} - 1 \right| &= \left| \frac{\widehat{P}_n(A_{j\ell})}{\mathbb{P}(A_{j\ell})} - 1 \right| = \frac{1}{p_{j\ell}} O_p \left(\left[\frac{p_{j\ell}(1-p_{j\ell})}{n} \right]^{1/2} \right) \\ &= O_p \left(\left[\frac{(1-p_{j\ell})}{np_{j\ell}} \right]^{1/2} \right) = O_p \left(\left[\frac{(1-c_0/k)}{nc_0/k} \right]^{1/2} \right) = O_p \left(\left(\frac{k}{n} \right)^{1/2} \right) \end{aligned}$$

by assumption (B1) that $\min_{(j,\ell) \in E} \mathbb{P}(A_{j\ell}) \geq \frac{c_0}{k}$, which completes the proof.

□

B.2 Face Density

Let $p(x)$ be the density function of the data distribution, let μ_d be the Lebesgue measure on the d -dimensional Euclidean space, let $F_{j\ell} = \bar{\mathbb{C}}_\ell \cap \bar{\mathbb{C}}_j$ denote the face between knots c_j, c_ℓ , and let $\partial F_{j\ell}$ be the boundary of $F_{j\ell}$. We consider the following assumptions: Again, we recall the assumptions:

(D1) (Density conditions) The PDF p has compact support \mathcal{X} , is bounded away from zero that $\inf_{x \in \mathcal{X}} p(x) \geq p_{\min} > 0$, $\sup_{x \in \mathcal{X}} p(x) \leq p_{\max} < \infty$, and is Lipschitz continuous.

(B2) There exist constants c_0, c_1 such that the face area

$$\frac{c_0}{k^{1-\frac{1}{d}}} \leq \min_{(j,\ell) \in E} \mu_{d-1}(F_{j\ell}) \leq \max_{(j,\ell) \in E} \mu_{d-1}(F_{j\ell}) \leq \frac{c_1}{k^{1-\frac{1}{d}}}$$

(B3) There exists a constant c_2 such that $\max_{(j,\ell) \in E} \mu_{d-2}(\partial F_{j\ell}) \leq \frac{c_2}{k^{1-\frac{2}{d}}}$,

(B4) There is an angle $\theta_0 < \pi$ such that, for every pair of intersecting face regions F_{ij} and $F_{j\ell}$, the maximal principle angle between the two subspaces $\theta_{ij,j\ell}$ satisfies $\theta_{ij,j\ell} \leq \theta_0$

(K1) (Kernel function conditions) The kernel function K is a positive and symmetric function satisfying $\int K^2(x)dx < \infty$, $\int |x|K(x)dx < \infty$, $\int x^2K(x)dx < \infty$.

PROOF OF THEOREM 2.

Our analysis starts with the usual bias-variance decomposition that

$$\widehat{S}_{j\ell}^{FD} - S_{j\ell}^{FD} = \underbrace{\widehat{S}_{j\ell}^{FD} - \mathbb{E}(\widehat{S}_{j\ell}^{FD})}_{\text{stochastic variation}} + \underbrace{\mathbb{E}(\widehat{S}_{j\ell}^{FD}) - S_{j\ell}^{FD}}_{\text{bias}}.$$

We analyze the two term separately. Before we start our proof, we first recall some useful notations.

Recall that the face region between two knots c_j, c_ℓ is $F_{j\ell} \equiv \overline{\mathbb{C}}_j \cap \overline{\mathbb{C}}_\ell$ and $c_* = c_j + \frac{1}{2}(c_\ell - c_j) = \frac{1}{2}(c_\ell + c_j)$ and $\mathbb{L}_{j\ell} = \{c_j - a(c_\ell - c_j) : a \in [0, 1]\}$ is the central line passing through c_j and c_ℓ , and for a value $a \in [0, 1]$. The face $F_{j\ell} = \{x \in \overline{\mathbb{C}}_j \cup \overline{\mathbb{C}}_\ell : \Pi_{j\ell}(x) = c_*\}$, where $\Pi_{j\ell}$ denotes the projection onto $\mathbb{L}_{j\ell}$. The quantity $\mu_s(dx)$ denotes the integration with respect to s -dimensional volume. We now reparametrize any point in $\mathbb{L}_{j\ell}$ using a unit distance t . Let $T_{j\ell,t} = \{x \in \mathcal{X} : \Pi_{j\ell}(x) = c_* + t \frac{c_\ell - c_j}{\|c_\ell - c_j\|}\}$ be the subspace orthogonal to $\mathbb{L}_{j\ell}$ at the point $c_* + t \frac{c_\ell - c_j}{\|c_\ell - c_j\|}$. t is 1-dimensional distance to c_* along the line passing through c_j and c_ℓ . Let

$$q_{j\ell}(t) = \int_{(\overline{\mathbb{C}}_j \cup \overline{\mathbb{C}}_\ell) \cap T_{j\ell,t}} p(x) \mu_{d-1}(dx)$$

With these quantities, $S_{j\ell}^{FD} = q_{j\ell}(0)$ and that $q_{j\ell}(t)$ is a 1-dimensional quantity. Our estimator is

$$\widehat{S}_{j\ell}^{FD} = \frac{1}{nh} \sum_{i=1}^n K\left(\frac{\Pi_{j\ell}(X_i) - c_*}{h}\right) I(X_i \in \overline{\mathbb{C}}_j \cup \overline{\mathbb{C}}_\ell).$$

Bias: We study the bias part first. A direct computation shows that

$$\mathbb{E}[\widehat{S}_{j\ell}^{FD}] = \mathbb{E}\left(\frac{1}{nh} \sum_{i=1}^n K\left(\frac{\Pi_{j\ell}(X_i) - c_*}{h}\right) I(X_i \in \overline{\mathbb{C}}_j \cup \overline{\mathbb{C}}_\ell)\right) \quad (6)$$

$$= \frac{1}{h} \int_{x \in \mathcal{X}} K\left(\frac{\Pi_{j\ell}(x) - c_*}{h}\right) I(x \in \overline{\mathbb{C}}_j \cup \overline{\mathbb{C}}_\ell) p(x) \mu_d(dx) \quad (7)$$

$$= \frac{1}{h} \int_{\mathbb{L}_{j\ell}} K\left(\frac{c_* + t \frac{c_\ell - c_j}{\|c_\ell - c_j\|} - c_*}{h}\right) \left(\int_{(\overline{\mathbb{C}}_j \cup \overline{\mathbb{C}}_\ell) \cap T_{j\ell,t}} p(y) \mu_{d-1}(dy)\right) d\left(c_j + t \frac{c_\ell - c_j}{\|c_\ell - c_j\|}\right) \quad (8)$$

$$= \frac{1}{h} \int_{\mathbb{R}} K\left(\frac{\|t \frac{c_\ell - c_j}{\|c_\ell - c_j\|}\|}{h}\right) q_{j\ell}(t) dt \quad (9)$$

$$= \frac{1}{h} \int_{\mathbb{R}} K\left(\frac{t}{h}\right) q_{j\ell}(t) dt \quad (10)$$

$$= \int_{\mathbb{R}} K(u) q_{j\ell}(hu) du, \quad (11)$$

where for the third equality, we split the integration with respect to $c_j + t \frac{c_\ell - c_j}{\|c_\ell - c_j\|} \in \mathbb{L}_{j\ell}$ and the integration with respect to the subspace orthogonal to $\mathbb{L}_{j\ell}$ at $c_j + t \frac{c_\ell - c_j}{\|c_\ell - c_j\|}$. This is possible because all the points in $T_{j\ell,t}$ have the same projection onto $\mathbb{L}_{j\ell}$. For

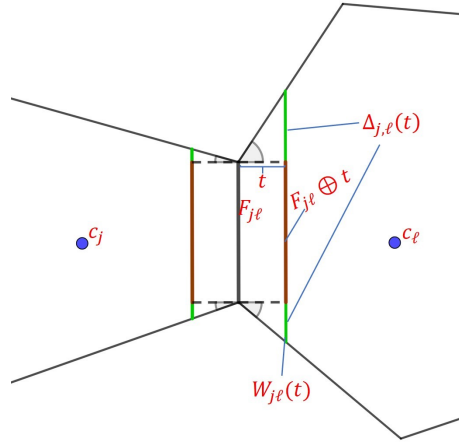


Figure 20: Decomposition of $W_{j\ell}(t)$. The dark red segment is $F_{j\ell} \oplus t$, which has the same shape with $F_{j\ell}$. The green segments consist $\Delta_{j,\ell}(t)$, the part leading to geometric bias.

the forth equality, we used the symmetry of the kernel function. the property of the kernel function that $K(x) = K(\|x\|)$. For the last equality, we used the change of variable that $u = \frac{t}{h}$ and got the simplified form.

The expansion of

$$q_{j\ell}(t) = \int_{(\bar{\mathbb{C}}_j \cup \bar{\mathbb{C}}_\ell) \cap T_{j\ell,t}} p(y) \mu_{d-1}(dy)$$

is more involved when $t \approx 0$. Let

$$\begin{aligned} W_{j\ell}(t) &= (\bar{\mathbb{C}}_j \cup \bar{\mathbb{C}}_\ell) \cap T_{j\ell,t} \\ &= \begin{cases} \bar{\mathbb{C}}_j \cap T_{j\ell,t}, & t < 0, \\ \bar{\mathbb{C}}_\ell \cap T_{j\ell,t}, & t > 0, \\ (\bar{\mathbb{C}}_j \cup \bar{\mathbb{C}}_\ell) \cap T_{j\ell,0} = F_{j\ell}, & t = 0 \end{cases} \end{aligned}$$

be the region that leads to $q_{j\ell}(t)$. For a face $F_{j\ell}$ and a real number $t \in \mathbb{R}$, we denote

$$F_{j\ell} \oplus t = \left\{ x + t \frac{c_\ell - c_j}{\|c_\ell - c_j\|} : x \in F_{j\ell} \right\}.$$

By the above notation, we can decompose

$$W_{j\ell}(t) = [F_{j\ell} \oplus t] \cup \Delta_{j,\ell}(t),$$

where $\Delta_{j,\ell}(t)$ is the additional region when moving away from $t = 0$; see Figure 20 for an example.

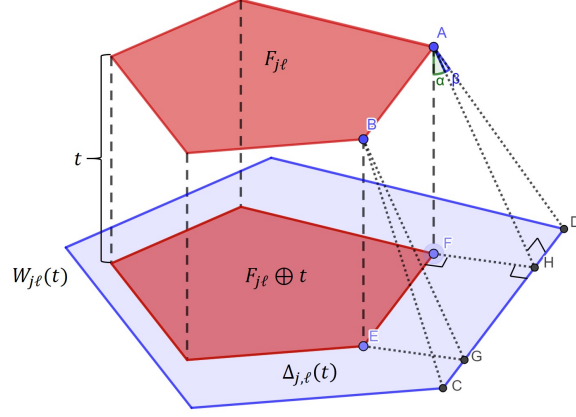


Figure 21: Decomposition of $W_{j\ell}(t)$. The red regions are $F_{j\ell}$ and the projected $F_{j\ell} \oplus t$, while the blue band region denotes $\Delta_{j,\ell}(t)$. All the α angles such as $\angle FAH$ and all the β angles such as $\angle HAD$ are bounded by θ_0 from assumption (B4).

Thus, the difference

$$\begin{aligned}
q_{j\ell}(hu) - q_{j\ell}(0) &= \int_{W_{j\ell}(hu)} p(y)\mu_{d-1}(dy) - \int_{W_{j\ell}(0)} p(y)\mu_{d-1}(dy) \\
&= \underbrace{\int_{F_{j\ell} \oplus hu} p(y)\mu_{d-1}(dy) - \int_{F_{j\ell}} p(y)\mu_{d-1}(dy)}_{(I)} + \underbrace{\int_{\Delta_{j\ell}(hu)} p(y)\mu_{d-1}(dy)}_{(II)}.
\end{aligned}$$

(I) is the usual bias caused by the change of density. Note that the Lipschitz condition in (D1) implies that there is a constant C_g such that $|p(x_1) - p(x_2)| \leq C_g|x_1 - x_2|$. Since every point can be matched nicely between $F_{j\ell} \oplus hu$ and $F_{j\ell}$, it can be bounded by

$$|(I)| \leq \mu_{d-1}(F_{j\ell})C_g h|u|.$$

(II) is the bias due to the change of volume, so we call it a geometric bias. With an upper bound of the density, (II) can be bounded by $(II) \leq \mu_{d-1}(\Delta_{j,\ell}(hu)) \cdot p_{max}$. Thus, we only need to bound the volume $\mu_{d-1}(\Delta_{j,\ell}(hu))$.

$\Delta_{j,\ell}(t)$ is illustrated by the blue region in Figure 21. The width of the band region like FH will all be bounded by $t \tan(\theta_0) = O(t)$, and as $t \rightarrow 0$ the surface area (circumference) will be bounded by $O(\mu_{d-2}(\partial F_{j\ell}))$.

Thus, the volume of the blue region $\mu_{d-1}(\Delta_{j,\ell}(t)) \leq O(\mu_{d-2}(\partial F_{j\ell})t)$, which leads to the bound

$$(II) \leq O(h|u| \cdot \mu_{d-2}(\partial F_{j\ell})) \cdot p_{max}.$$

Putting altogether, we have

$$|q_{j\ell}(hu) - q_{j\ell}(0)| \leq \mu_{d-1}(F_{j\ell})C_g h|u| + p_{max}h|u| \cdot O(\mu_{d-2}(\partial F_{j\ell}) \tan(\theta_0)) \quad (12)$$

This, together with equation (11), implies that

$$\begin{aligned} |\mathbb{E}[\widehat{S}_{j\ell}^{FD}] - \underbrace{q_{j\ell}(0)}_{=S_{j\ell}^{FD}}| &= \left| \int_{\mathbb{R}} K(u)[q_{j\ell}(hu) - q_{j\ell}(0)]du \right| \\ &\leq \int_{\mathbb{R}} K(u)|q_{j\ell}(hu) - q_{j\ell}(0)|du \\ &\leq h \left[\int_{\mathbb{R}} |u|K(u)du \right] \times \left[\mu_{d-1}(F_{j\ell})C_g + p_{max}O(\mu_{d-2}(\partial F_{j\ell})) \right] \\ &\stackrel{(B2-3)}{=} O\left(h \cdot \left[\frac{1}{k^{1-1/d}}\right]\right) + O\left(h \cdot \left[\frac{1}{k^{1-2/d}}\right]\right) \end{aligned}$$

As a result,

$$|\mathbb{E}[\widehat{S}_{j\ell}^{FD}] - S_{j\ell}^{FD}| = O\left(\frac{h}{k^{1-1/d}}\right) + O\left(\frac{h}{k^{1-2/d}}\right) \quad (13)$$

Moreover, note that

$$\frac{h}{k^{1-1/d}} \times \frac{k^{1-2/d}}{h} = \frac{1}{k^{1/d}} \rightarrow 0 \quad (14)$$

since $k \rightarrow \infty$. Therefore the bias given by the geometric difference (II) dominates the bias given by the change in density (I). Even if we assume a higher order derivative, the bias in (II) will still dominate the component in (I).

Therefore, the overall bias can be expressed as reduces to

$$|\mathbb{E}[\widehat{S}_{j\ell}^{FD}] - S_{j\ell}^{FD}| = O\left(\frac{h}{k^{1-2/d}}\right) \quad (15)$$

Stochastic variation: For the stochastic variation part, we have

$$\begin{aligned}
\text{Var}(\widehat{S}_{j\ell}^{FD}) &= \text{Var}\left(\frac{1}{nh} \sum_{i=1}^n K\left(\frac{\Pi_{j\ell}(X_i) - c_*}{h}\right) I(X_i \in \overline{\mathcal{C}}_j \cup \overline{\mathcal{C}}_\ell)\right) \\
&\leq \frac{1}{nh^2} \mathbb{E}\left[K^2\left(\frac{\Pi_{j\ell}(X_i) - c_*}{h}\right) I(X_i \in \overline{\mathcal{C}}_j \cup \overline{\mathcal{C}}_\ell)\right] \\
&\leq \frac{1}{nh} \int K^2(u) \left(q_{j\ell}(0) + \mu_{d-1}(F_{j\ell})C_g + p_{max}h|u|\mu_{d-2}(\partial F_{j\ell})\tan(\theta_0)\right) du \\
&\leq \frac{1}{nh} \int K^2(u) \left(q_{j\ell}(0) + O\left(\frac{h}{k^{1-1/d}}\right) + O\left(\frac{h}{k^{1-2/d}}\right)\right) du
\end{aligned} \tag{16}$$

by the same decomposition in (11) and the bound in (12) and the assumptions (K1). Note that similar to (14), the second term in (16) is at a slower rate than the third term, so we can simplify it as

$$\text{Var}(\widehat{S}_{j\ell}^{FD}) = O\left(\frac{q_{j\ell}(0)}{nh}\right) + O\left(\frac{1}{nk^{1-2/d}}\right). \tag{17}$$

Combining (13) and (16), we conclude that for $\forall j, \ell$,

$$|\widehat{S}_{j\ell}^{FD} - S_{j\ell}^{FD}| = O\left(\frac{h}{k^{1-2/d}}\right) + O_p\left(\sqrt{\frac{q_{j\ell}(0)}{nh}}\right) + O_p\left(\sqrt{\frac{1}{nk^{1-2/d}}}\right) \tag{18}$$

Note that the volume of face region $F_{j\ell}$ decreases when k increases. By assumption (D1) and (B2), we have

$$q_{j\ell}(0) = S_{j\ell}^{FD} \geq p_{\min} \min_{(j,\ell) \in E} \mu_{d-1}(F_{j\ell}) = p_{\min} \frac{c_0}{k^{1-\frac{1}{d}}}. \tag{19}$$

For the theorem we again take the ratio between the estimated and the true face density to accommodate the fact that the true face density is decreasing with number of knots, and we have that This implies that

$$\left|\frac{\widehat{S}_{j\ell}^{FD}}{S_{j\ell}^{FD}} - 1\right| = O(hk^{1/d}) + O_p\left(\sqrt{\frac{k^{1-\frac{1}{d}}}{nh}}\right) + O_p\left(\sqrt{\frac{k}{n}}\right) \tag{20}$$

When $hk^{1/d} \rightarrow 0$,

$$\frac{k^{1-\frac{1}{d}}}{nh} \times \frac{n}{k} = \frac{1}{hk^{1/d}} \rightarrow \infty, \tag{21}$$

so the second term dominates the third term in (20) and the rate reduces to

$$\left| \frac{\widehat{S}_{j\ell}^{FD}}{S_{j\ell}^{FD}} - 1 \right| = O(hk^{1/d}) + O_p\left(\sqrt{\frac{k^{1-\frac{1}{d}}}{nh}}\right), \quad (22)$$

which completes the proof.

□

B.3 Tube Density Consistency

We consider the following assumptions, which are slightly stronger than those in the case of the FD:

- (D2) (Density conditions) The PDF p has compact support, is in the 3-Hölder class, and $\inf_{x \in \mathcal{X}} p(x) \geq f_{\min} > 0$.
- (D3) (Disk Density conditions) For any pair c_j, c_ℓ , the minimum disk density location $t^* = \operatorname{argmin}_{t \in [0,1]} \mathbf{pDisk}_{j\ell,R}(t) \in (0, 1)$ is unique and satisfies $\mathbf{pDisk}_{j\ell,R}^{(2)}(t^*) \geq c_{\min} > 0$.
- (K2) (Kernel function conditions) The kernel function K is a positive and symmetric function satisfying $\int x^2 K^{(\alpha)}(x) dx < \infty$, $\int (K^{(\alpha)}(x))^2 dx < \infty$, for all $\alpha = 0, 1, 2$, where $K^{(\alpha)}$ denotes the α -th order derivative of K .

PROOF OF THEOREM 3.

Let $t^* = \operatorname{argmin}_t \mathbf{pDisk}_{j\ell,R}(t)$ and $\widehat{t}^* = \operatorname{argmin}_t \widehat{\mathbf{pDisk}}_{j\ell,R}(t)$. Then the tube densities

$$\begin{aligned} S_{j\ell}^{TD} &= \inf_{t \in [0,1]} \mathbf{pDisk}_{j\ell,R}(t) = \mathbf{pDisk}_{j\ell,R}(t^*), \\ \widehat{S}_{j\ell}^{TD} &= \inf_{t \in [0,1]} \widehat{\mathbf{pDisk}}_{j\ell,R}(t) = \widehat{\mathbf{pDisk}}_{j\ell,R}(\widehat{t}^*). \end{aligned}$$

Since the ratio difference

$$\frac{\widehat{S}_{j\ell}^{TD}}{S_{j\ell}^{TD}} - 1 = \frac{1}{S_{j\ell}^{TD}} \left(\widehat{S}_{j\ell}^{TD} - S_{j\ell}^{TD} \right),$$

we will focus on the difference $\widehat{S}_{j\ell}^{TD} - S_{j\ell}^{TD}$.

The difference admits the following decomposition:

$$\begin{aligned}
\widehat{S}_{j\ell}^{TD} - S_{j\ell}^{TD} &= \widehat{\text{pDisk}}_{j\ell,R}(\widehat{t}^*) - \text{pDisk}_{j\ell,R}(t^*) \\
&= \underbrace{\widehat{\text{pDisk}}_{j\ell,R}(\widehat{t}^*) - \widehat{\text{pDisk}}_{j\ell,R}(t^*)}_{(I)} + \underbrace{\widehat{\text{pDisk}}_{j\ell,R}(t^*) - \mathbb{E}(\widehat{\text{pDisk}}_{j\ell,R}(t^*))}_{(II)} \\
&\quad + \underbrace{\mathbb{E}(\widehat{\text{pDisk}}_{j\ell,R}(t^*)) - \text{pDisk}_{j\ell,R}(t^*)}_{(III)}.
\end{aligned}$$

It is easier to start with term (III) and then term (II) and then term (I).

Recall that

$$q_{v,R}(y) = \int_{\text{Disk}(y,R,v)} p(x) dx,$$

and hence $\text{pDisk}_{j\ell,R}(t) = q_{c_\ell - c_j, R}(c_j - t(c_\ell - c_j))$.

(III): Bias. Note that the kernel weights $w(x) = K\left(\frac{\Pi_{j\ell}(x) - c_j - t(c_\ell - c_j)}{h}\right)$ is the same for all $x \in \text{Disk}(c_j - t(c_\ell - c_j), R, c_\ell - c_j)$. Let $\mathbb{L}_{j\ell} = \{c_j - t(c_\ell - c_j) : t \in \mathbb{R}\}$ be the line passing through c_j and c_ℓ . Then

$$\begin{aligned}
\mathbb{E}[\widehat{\text{pDisk}}_{j\ell,R}(t)] &= \mathbb{E}\left(\frac{1}{nh} \sum_{i=1}^n K\left(\frac{\Pi_{j\ell}(X_i) - c_j - t(c_\ell - c_j)}{h}\right) I(\|X_i - \Pi_{j\ell}(X_i)\| \leq R)\right) \\
&= \frac{1}{h} \int_{x \in \mathcal{X}} K\left(\frac{\Pi_{j\ell}(x) - c_j - t(c_\ell - c_j)}{h}\right) I(\|x - \Pi_{j\ell}(x)\| \leq R) p(x) \mu_d(dx) \\
&= \frac{1}{h} \int_{\mathbb{L}_{j\ell}} K\left(\frac{z - c_j - t(c_\ell - c_j)}{h}\right) \left(\int_{\text{Disk}(z,R,c_\ell - c_j)} p(y) \mu_{d-1}(dy)\right) dz \\
&= \frac{1}{h} \int_{\mathbb{L}_{j\ell}} K\left(\frac{z - c_j - t(c_\ell - c_j)}{h}\right) q_{c_\ell - c_j, R}(z) dz \\
&= \frac{\|c_j - c_\ell\|}{h} \int_{\mathbb{L}_{j\ell}} K\left(\frac{(s-t)\|c_j - c_\ell\|}{h}\right) q_{c_\ell - c_j, R}(c_j - s(c_\ell - c_j)) ds
\end{aligned}$$

where for the third equality we split the integration with respect to $z \in \mathbb{L}_{j\ell}$ and the integration with respect to $y \in \text{Disk}(z, R, c_\ell - c_j)$, and for the last equality we set $z = c_j - s(c_\ell - c_j)$ and utilized the symmetry of the kernel function K .

Then by another change of variable that $u = \frac{(s-t)\|c_j - c_\ell\|}{h}$ and Taylor expansion, we have

$$\begin{aligned}
\mathbb{E}[\widehat{\text{pDisk}}_{j\ell,R}(t)] &= \int K(u) q_{c_\ell - c_j, R}\left(c_j - t(c_\ell - c_j) - hu \frac{c_\ell - c_j}{\|c_j - c_\ell\|}\right) du \\
&= \int K(u) \left(q_{c_\ell - c_j, R}(c_j - t(c_\ell - c_j)) + hu \cdot g_1 + \frac{1}{2} h^2 u^2 \cdot g_2 + O(h^2)\right) du
\end{aligned}$$

where

$$g_1 = \left(\frac{c_\ell - c_j}{\|c_j - c_\ell\|} \right)^T \cdot \nabla q_{c_\ell - c_j, R}(c_j - t(c_\ell - c_j))$$

$$g_2 = \left(\frac{c_\ell - c_j}{\|c_j - c_\ell\|} \right)^T \cdot \nabla \nabla q_{c_\ell - c_j, R}(c_j - t(c_\ell - c_j)) \left(\frac{c_\ell - c_j}{\|c_j - c_\ell\|} \right)$$

When $R \rightarrow 0$, assumption (D2) implies that there is a constant C_{d-1} that

$$2p_{\min} C_{d-1} R^{d-1} \leq \mathbf{pDisk}_{j\ell, R}(t) \leq 2p_{\max} C_{d-1} R^{d-1} = O(R^{d-1}) \quad (23)$$

where $0 < p_{\min} \leq \inf_{x \in \mathcal{X}} p(x)$, $\sup_{x \in \mathcal{X}} p(x) \leq p_{\max} < \infty$. Since the disk density is shrinking at rate $O(R^{d-1})$, one can easily verify that the gradient and Hessian of the disk density function is also at rate $O(R^{d-1})$. Namely,

$$g_1 = O(R^{d-1}), \quad g_2 = O(R^{d-1}).$$

By assumption (D2) we have g_1 and g_2 to be bounded and therefore Thus,

$$\begin{aligned} \mathbb{E}[\widehat{\mathbf{pDisk}}_{j\ell, R}(t)] &= q_{c_\ell - c_j, R}(c_j - t(c_\ell - c_j)) \int K(u) du + h \left[\int u K(u) du \right] \cdot g_1 \\ &\quad + \frac{1}{2} h^2 \left[\int u^2 K(u) du \right] \cdot g_2 + O(h^2 R^{d-1}) \\ &= q_{c_\ell - c_j, R}(c_j - t(c_\ell - c_j)) + O(h^2 R^{d-1}) \\ &= \mathbf{pDisk}_{j\ell, R}(t) + O(h^2 R^{d-1}), \end{aligned}$$

where for the second equality we used, by assumption (K)

$$\int K(u) du = 1, \quad \int u K(u) du = 0, \quad \int u^2 K(u) du < \infty$$

so we conclude that $|\mathbb{E}[\widehat{\mathbf{pDisk}}_{j\ell, R}(t)] - \mathbf{pDisk}_{j\ell, R}(t)| = O(h^2 R^{d-1})$

(II): Stochastic variation.

$$\begin{aligned}
\text{Var}(\widehat{\text{pDisk}}_{j\ell,R}(t)) &= \text{Var}\left(\frac{1}{nh} \sum_{i=1}^n K\left(\frac{\Pi_{j\ell}(X_i) - c_j - t(c_\ell - c_j)}{h}\right) I(\|X_i - \Pi_{j\ell}(X_i)\| \leq R)\right) \\
&\leq \frac{1}{nh^2} \mathbb{E}\left[K^2\left(\frac{\Pi_{j\ell}(X_i) - c_j - t(c_\ell - c_j)}{h}\right) I(\|X_i - \Pi_{j\ell}(X_i)\| \leq R)\right] \\
&= \frac{1}{nh} \int K^2(u) \left(q_{c_\ell - c_j, R}(c_j - t(c_\ell - c_j)) + hu \cdot g_1 + O(h^2)\right) du \\
&= O\left(\frac{1}{nh}\right)
\end{aligned}$$

by the same analysis procedure as for Face Density and the assumptions (D1), (K1).

Now, by assumption (D2), the face density $q_{c_\ell - c_j, R}(c_j - t(c_\ell - c_j)) = O(R^{d-1})$, which leads to

$$\text{Var}(\widehat{\text{pDisk}}_{j\ell,R}(t)) = O\left(\frac{R^{d-1}}{nh}\right).$$

Therefore,

$$|\widehat{\text{pDisk}}_{j\ell,R}(t) - \mathbb{E}[\widehat{\text{pDisk}}_{j\ell,R}(t)]| = O_p\left(\sqrt{\frac{R^{d-1}}{nh}}\right)$$

and

$$|\widehat{\text{pDisk}}_{j\ell,R}(t) - \text{pDisk}_{j\ell,R}(t)| = O(h^2 R^{d-1}) + O_p\left(\sqrt{\frac{R^{d-1}}{nh}}\right). \quad (24)$$

(I): Change in position. Finally, we bound the term

$$(I) = \widehat{\text{pDisk}}_{j\ell,R}(\widehat{t}^*) - \widehat{\text{pDisk}}_{j\ell,R}(t^*).$$

Note that the minimizer \widehat{t}^* satisfies the gradient condition

$$\widehat{\text{pDisk}}'_{j\ell,R}(\widehat{t}^*) = 0.$$

By a simple Taylor expansion at \widehat{t}^* , we obtain

$$\begin{aligned}
(I) &= -(\widehat{\text{pDisk}}_{j\ell,R}(t^*) - \widehat{\text{pDisk}}_{j\ell,R}(\widehat{t}^*)) \\
&= -(t^* - \widehat{t}^*) \underbrace{\widehat{\text{pDisk}}'_{j\ell,R}(\widehat{t}^*)}_{=0} - \frac{1}{2}(t^* - \widehat{t}^*)^2 \widehat{\text{pDisk}}''_{j\ell,R}(\widehat{t}^*) + O(|t^* - \widehat{t}^*|^3) \\
&= O(|t^* - \widehat{t}^*|^2).
\end{aligned}$$

Thus, we only need to derive the rate of $t^* - \widehat{t}^*$.

Now by the fact that t^* solves the population gradient condition $\mathfrak{p}\text{Disk}'_{j\ell,R}(t^*) = 0$, we have

$$\begin{aligned}\widehat{\mathfrak{p}\text{Disk}}'_{j\ell,R}(t^*) - \mathfrak{p}\text{Disk}'_{j\ell,R}(t^*) &= \widehat{\mathfrak{p}\text{Disk}}'_{j\ell,R}(t^*) - \widehat{\mathfrak{p}\text{Disk}}'_{j\ell,R}(\widehat{t}^*) \\ &= \widehat{\mathfrak{p}\text{Disk}}''_{j\ell,R}(t^*)(t^* - \widehat{t}^*) + O(|t^* - \widehat{t}^*|^2).\end{aligned}$$

Because $\widehat{\mathfrak{p}\text{Disk}}''_{j\ell,R}(t^*) \xrightarrow{P} \mathfrak{p}\text{Disk}''_{j\ell,R}(t^*)$ from the analysis of term (II) and (III), we conclude that

$$\widehat{t}^* - t^* = O(\widehat{\mathfrak{p}\text{Disk}}'_{j\ell,R}(t^*) - \mathfrak{p}\text{Disk}'_{j\ell,R}(t^*)) = O(h^2 R^{d-1}) + O_P\left(\sqrt{\frac{R^{d-1}}{nh^3}}\right).$$

Note that the above rate analysis follows from the same analysis as term (II) and (III) except that we are using gradient rather than the density.

As a result, we conclude that

$$(I) = O(|t^* - \widehat{t}^*|^2) = O(h^4 R^{2d-2}) + O_P\left(\frac{R^{d-1}}{nh^3}\right).$$

Combining together, we have

$$\begin{aligned}|\widehat{S}_{j\ell}^{TD} - S_{j\ell}^{TD}| &= (I) + (II) + (III) \\ &= O(h^4 R^{2d-2}) + O_p\left(\frac{R^{d-1}}{nh^3}\right) + O(h^2 R^{d-1}) + O_p\left(\sqrt{\frac{R^{d-1}}{nh}}\right) \\ &= O(h^2 R^{d-1}) + O_p\left(\sqrt{\frac{R^{d-1}}{nh}}\right) + O_p\left(\frac{R^{d-1}}{nh^3}\right).\end{aligned}$$

Using the fact that $S_{j\ell}^{TD} \geq 2p_{\min} C_{d-1} R^{d-1}$ from equation (23), we conclude that

$$\left|\frac{\widehat{S}_{j\ell}^{TD}}{S_{j\ell}^{TD}} - 1\right| = O(h^2) + O_p\left(\sqrt{\frac{1}{nhR^{d-1}}}\right) + O_p\left(\frac{1}{nh^3}\right),$$

which completes the proof.

□

C Additional Data Analysis

C.1 Performance under Different Bandwidth Rate

In this section we present empirical results on how changing the bandwidth rate affects the performance of clustering. We consider the Yinyang data in Section 5.1.1 with $d = 10, 100, 500, 1000$. We compare the Face and Tube density where the bandwidth is selected by Silverman’s rule of thumb with different rates, ranging from $n_{loc}^{-1/3}$ to $n_{loc}^{-1/10}$. Note that the original Silverman’s rule of thumb will be at rate $n_{loc}^{-1/5}$. We repeat the experiment 100 times and record the adjust Rand index in Figure 22.

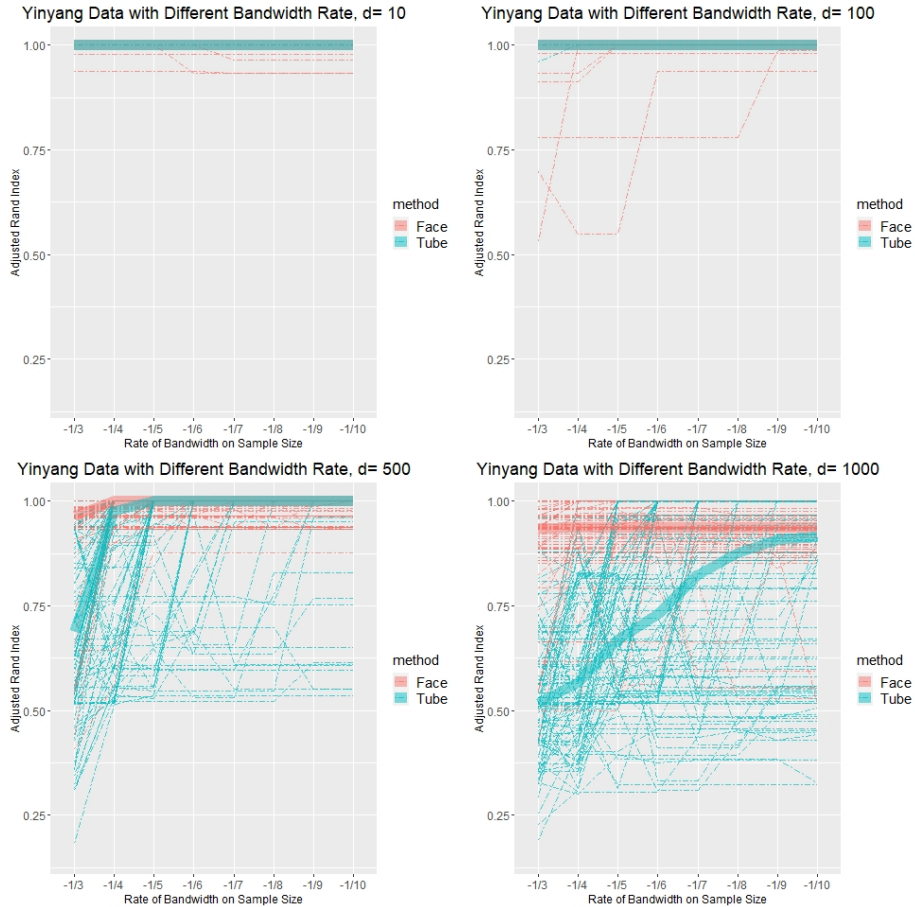


Figure 22: Adjusted Rand indexes of skeleton clustering with Face and Tube density under different bandwidth rate on 100 simulated Yinyang datasets. The thick lines indicate the median adjusted Rand index of a given method.

When the dimension is low (top panels), all bandwidth within this range works well. When the dimension is large (bottom panels), a slower rate (larger bandwidth) seems to be showing a better performance for the TD. Interestingly, the face density yields a robust result across different rates of bandwidth. Note that for the TD, the theory (Theorem 3) suggests the choice at rate $h \asymp n_{loc}^{-1/5}$ is optimal for estimation in large d , the same rate may not lead to a the optimal clustering performance. Figure 22

bottom-right panel suggests that the choice $h \asymp n_{loc}^{-1/10}$ may have a better clustering performance in this case.

C.2 Performance with Different Number of Knots

Next we analyze how the number of knots would affect the performance of the skeleton clustering. In Figure 23, we show the knot-size diagrams under different numbers of knots. This is based on the Yinyang data with $d = 200$. Note that our reference rule $k = \sqrt{n}$ takes 57 knots with the knot-size diagram shown in Figure 3.

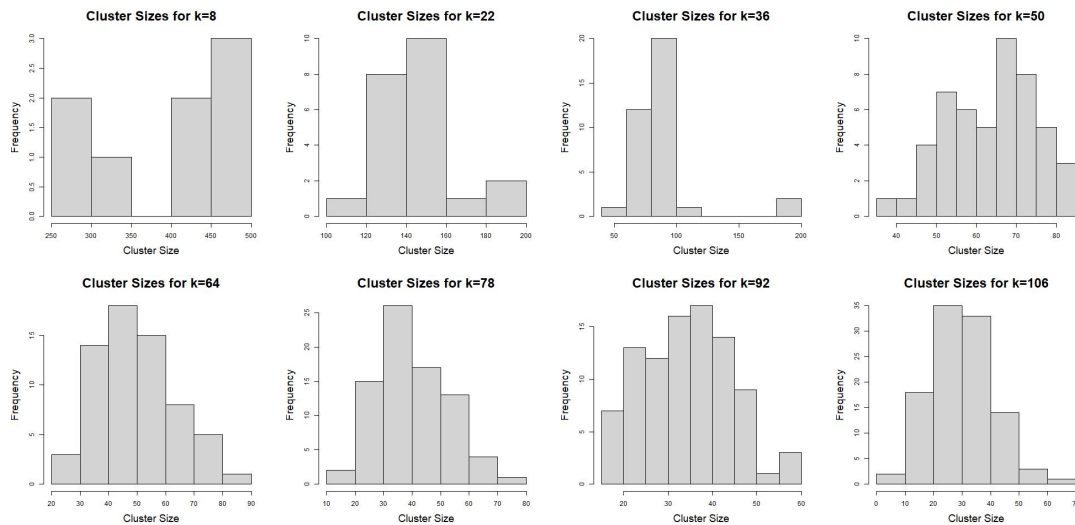


Figure 23: The knot-size diagram with different k on Yinyang data with dimension 200.

In addition to the knot-size diagrams, We empirically test the effect of the number of knots, k , on the final clustering performance on Yinyang data with dimensions 10, 100, 500 and 1000. For each dimension, we simulated the Yinyang data 100 times, and for each simulated data we carried out the default skeleton clustering procedure with different k (other steps the same as in Section 5.1.1). Figure 24 displays the median adjusted Rand index given by each method across different k , where the reference rule with $k = 57$ is marked by the vertical dash line. We see that as long as k is sufficiently large, skeleton clustering works well.

C.3 Self-Organizing Map

The Self-Organizing Map (SOM) is another popular prototype clustering method and can be used as an alternative to k -means clustering in finding knots. Thus, here we conduct a simple experiment to examine the performance of using SOM to find knots. We examine the performance using Yinyang data with $d = 10$ to $d = 1000$.

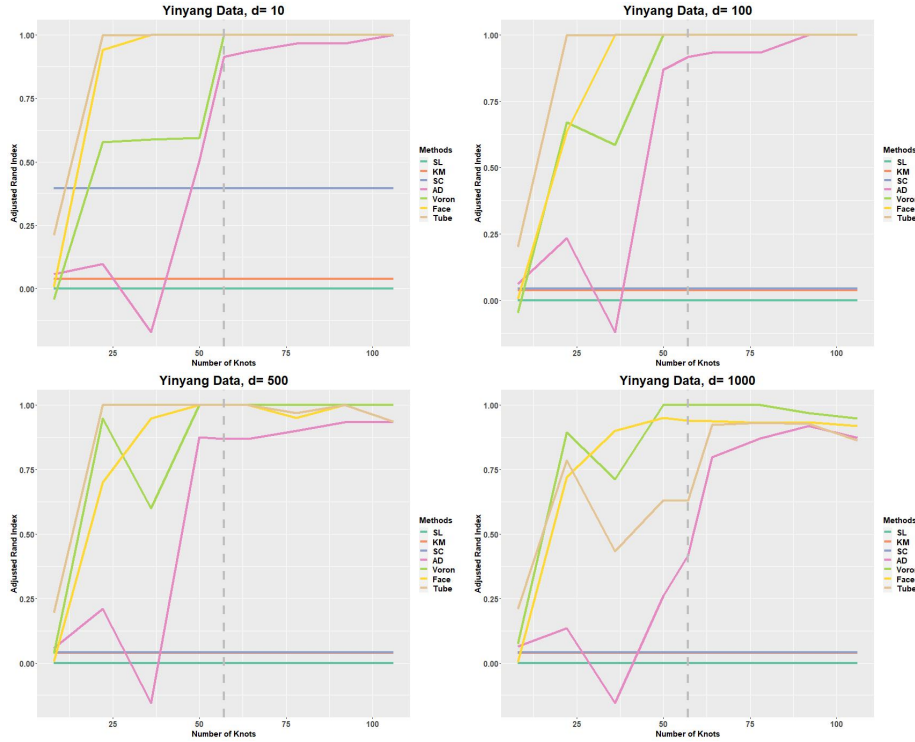


Figure 24: Adjusted Rand indexes of different clustering methods against different number of knots on 100 simulated Yinyang data.

The identical procedure as in Section 5.1.1 is applied except that the knots are now detected by the SOM rather than overfitting k -means. The total number of grid points in the SOM is the total number of knots we obtain and, to be comparable to k -means with $k = \sqrt{n}$ knots, we used $\lceil n^{1/4} \rceil$ breaks for each dimension of the SOM grid, giving a total of $\lceil n^{1/4} \rceil^2$ initial grid points. However, the SOM may return knots with very tiny sample size, on which the density-based similarity measures cannot be calculated. Therefore, we remove knots with less than 3 data points and use the remaining ones for skeleton construction.

Figure 25 summarizes the result. The top left panel shows the knots from the SOM (after post-processing), which are located around the main data structures and are representative to the original data as well. The dendrogram shows the cluster structure of the SOM knots using Voronoi density on one 100-dimensional Yinyang data. In the bottom row, we display the adjusted Rand indices from the clustering methods. Compared to the results of Figure 8, the adjusted Rand indices given by the skeleton clustering with SOM knots are similarly good when the dimension is not so high ($d = 10$ and 100). But when the data dimension becomes high ($d = 500, 1000$), knots constructed by SOM lead to worse clustering results. Therefore, overfitting k -means is favored in this work. Another limitation of SOM is that we need to perform

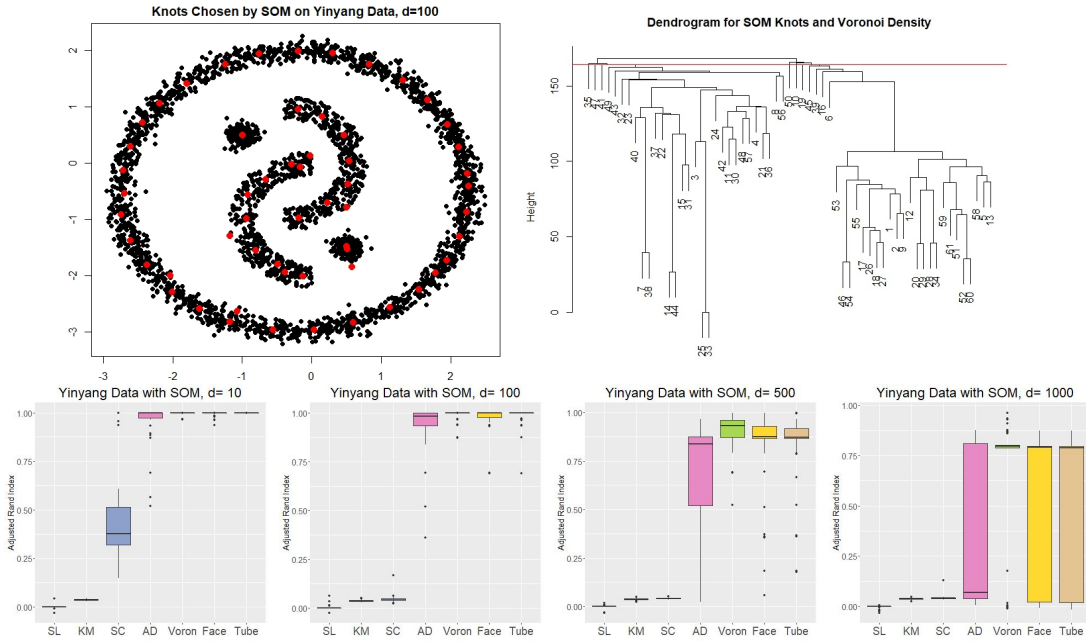


Figure 25: Adjusted Rand indexes using SOM for knots selection on Yinyang data.

some post-processing to remove tiny knots; in the case of k-means, we do not need such procedure.

C.4 Ring Data

The ring data is constructed by a mixture distribution such that with a probability of $\frac{1}{6}$ we sample from the ring structure and with a probability of $\frac{5}{6}$, we sample from the central part. The ring structure is generated by a uniform distribution over the ring $\{(x_1, x_2) : x_1^2 + x_2^2 = 1\}$ and is corrupted with an additive Gaussian noise $N(0, 0.2^2 \mathbf{I}_2)$. The central part is simply a Gaussian $N(0, 0.2^2 \mathbf{I}_2)$. We generate a total of $n = 1200$ points from the above mixture and add the high dimensional noise with the same procedure as in Section 5.1. The same skeleton clustering approaches are applied as well as the classical approaches, with the final number of clusters chosen to be 2. The result is displayed in Figure 27. Again, the density-based skeleton clustering methods work well even when the dimension is large.

C.5 Other linkage criteria for segmentation

In this section we compare the performance of knot segmentation using other popular linkage criteria. In particular, we focus on cases where clusters may be overlapped. We consider two scenarios: the mix Mickey data presented previously in Section 5.3 and another simulated mixed star data. The results are displayed in

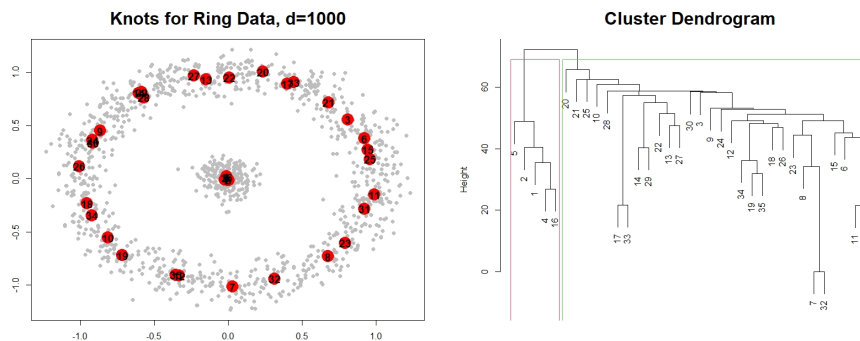


Figure 26: Results on Ring data with dimension 1000.

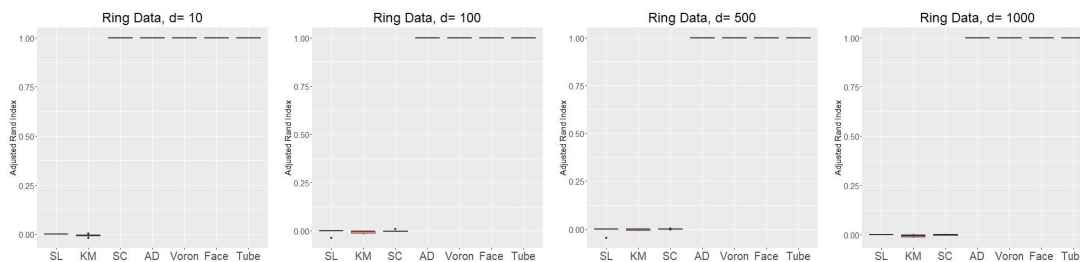


Figure 27: Comparison of the rand index using different similarity measures on Ring data with dimensions 10, 100, 500, 1000. Medium of 100 repetitions.

Figure 28 and 29. Clearly, we see that only the average linkage can reliably recover clusters when they are overlapping.

C.6 Olive Oil Data

Finally, we consider another real dataset; the the Olive Oil data (Tsimidou et al., 1987), a popular dataset for cluster analysis. This data set represents $d = 8$ chemical measurements on different specimens of olive oil produced in 9 different regions in Italy (northern Apulia, southern Apulia, Calabria, Sicily, inland Sardinia, and coast

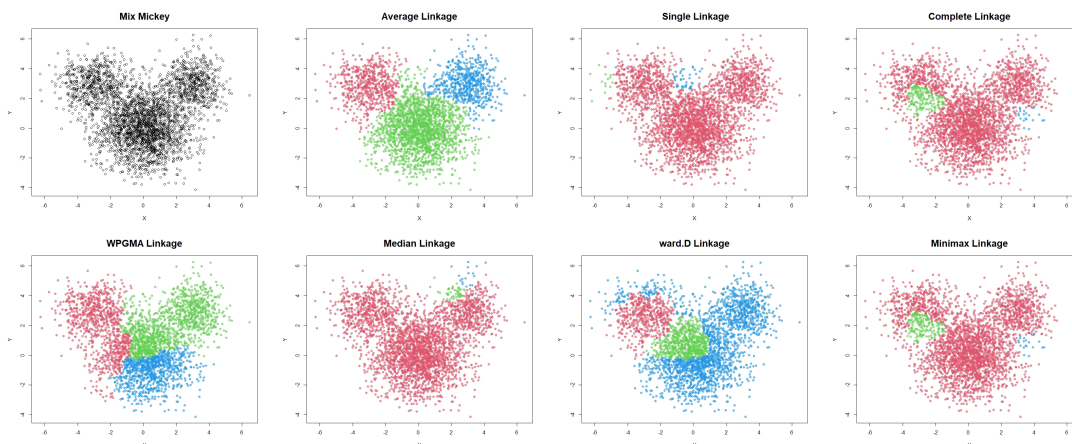


Figure 28: Comparing linkage criteria in segmentation on the mix Mickey data.

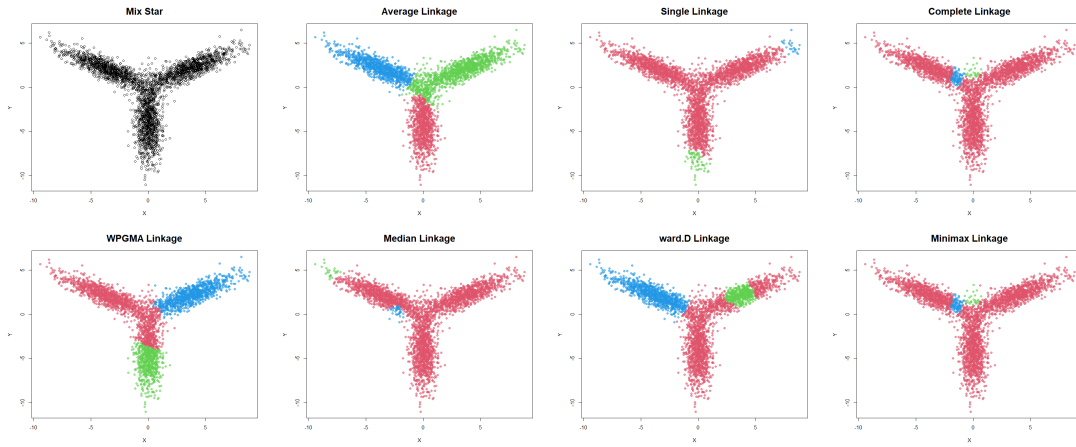


Figure 29: Comparing linkage criteria in segmentation on the mixed star data.

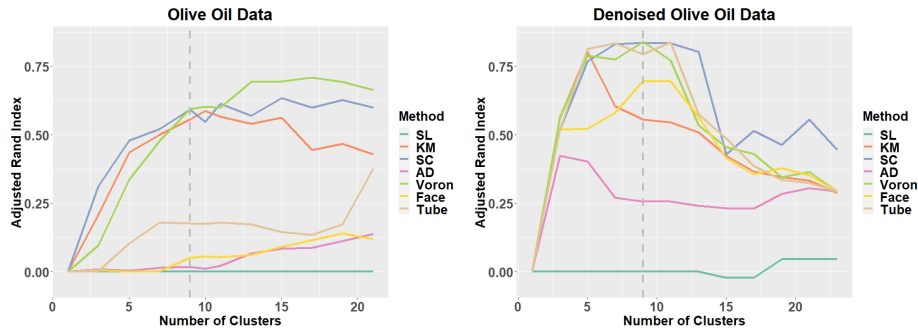


Figure 30: The clustering performance under different number of final clusters of the Olive oil data.

Sardinia, eastern and western Liguria, Umbria) . There are a total of $n = 572$ observations in the dataset.

The performance of different similarity measures is presented in Figure 30. Different color denotes different similarity measures and the gray vertical line indicates the actual number of clusters 9. Overall, the skeleton clustering with Voronoi density and Tube density works well; the spectral clustering also performs well in this case. The fact that average distance fails to capture clusters in the data highlights the importance of using a density-based similarity in this case. Note that we also include the clustering performance on the ‘denoised’ data, in which we remove the 10% observation with the lowest $\sqrt{n} - NN$ density estimate.